

Sediment yield, spatial characteristics, and the long-term evolution of active earthflows determined from airborne LiDAR and historical aerial photographs, Eel River, California

Benjamin H. Mackey[†], and Joshua J. Roering

Department of Geological Sciences, 1272 University of Oregon, Eugene, Oregon 97403, USA

ABSTRACT

In mountainous landscapes with weak, fine-grained rocks, earthflows can dominate erosion and landscape evolution by supplying sediment to channels and controlling hillslope morphology. To estimate the contribution of earthflows to regional sediment budgets and identify patterns of landslide activity, earthflow movement needs to be quantified over significant spatial and temporal scales. Presently, there is a paucity of data that can be used to predict earthflow behavior beyond the seasonal scale or over spatially extensive study areas. Across 226 km² of rapidly eroding Franciscan Complex rocks of the Eel River catchment, northern California, we used a combination of LiDAR (light detection and ranging) and orthorectified historical aerial photographs to objectively map earthflow movement between 1944 and 2006. By tracking the displacement of trees growing on earthflow surfaces, we find that 7.3% of the study area experienced movement over this 62 yr interval, preferentially in sheared argillaceous lithology. This movement is distributed across 122 earthflow features that have intricate, elongate planform shapes, a preferred south-southwesterly aspect, and a mean longitudinal slope of 31%. The distribution of mapped earthflow areas is well-approximated by a lognormal distribution with a median size of 36,500 m². Approximately 6% of the study area is composed of earthflows that connect to major channels; these flows generated an average sediment yield of 19,000 t km⁻² yr⁻¹ (rock erosion rate of ~7.6 mm/yr) over the 62 yr study

period, equating to a regional yield of 1100 t km⁻² yr⁻¹ (~0.45 mm/yr) if distributed across the study area. As such, a small fraction of the landscape can account for half of the regional denudation rate estimated from suspended sediment records (2200 t km⁻² yr⁻¹ or ~0.9 mm/yr). We propose a conceptual model for long-term earthflow evolution wherein earthflows experience intermittent activity and long periods of dormancy when limited by the availability of readily mobilized sediment on upper slopes. Ultimately, high-order river channels and ephemeral gully networks may serve to destabilize hillslopes, controlling the evolution of earthflow-prone terrain.

INTRODUCTION

Earthflows

In mountainous landscapes without active glaciers, sediment production and hillslope form are primarily controlled by mass-wasting processes, including slow-moving, deep-seated landslides known as earthflows. These large slope failures can establish or modify drainage patterns, alter hillslope morphology, and impart large perturbations on sediment budgets by regulating the timing, magnitude, frequency, spatial distribution, and grain size of sediment entering a channel or river network (Hovius et al., 1998; Korup, 2005b, 2006). This has direct implications for flooding, channel network evolution, sediment transport, aquatic habitat, and infrastructure. While the importance of landsliding in mountainous landscapes has been long recognized, we are still challenged to understand and quantify the ways in which landslides, and in particular earthflows, modulate the rate and locations of sediment flux, and control landscape form, over geomorphically significant time scales (Dietrich et al., 2003; Korup et al., 2010).

Slow-moving earthflows are a class of landslide (Cruden and Varnes, 1996) characterized

by sliding along transient shear surfaces with a degree of internal deformation or flow. They span a range of landslide failure styles and have been variably described as landslide complexes (Iverson, 1986a), landslides (Schulz et al., 2009b), earth slides (Cruden and Varnes, 1996), and mudslides (Chandler and Brunsden, 1995; Glastonbury and Fell, 2008). Hereafter, we use the term earthflow as advocated by Hungr et al. (2001) to describe large, slow-moving landslides with macroscale, flow-like morphology. These features morphologically resemble “earth glaciers.” They are generally slow moving (<4 m/yr), large (>500 m long), deep seated (>5 m thick), and mechanically dominated by fine-grained material, and they behave in a plastic or visco-plastic manner (e.g., Putnam and Sharp, 1940; Kelsey, 1978; Iverson and Major, 1987; Zhang et al., 1991b; Bovis and Jones, 1992; Baum et al., 1993; Chandler and Brunsden, 1995; Malet et al., 2002; Coe et al., 2003; Mackey et al., 2009). Earthflows classically have an hourglass planform shape, with an amphitheater-like source zone, an elongate narrow transport zone, and a lobate compressional toe or depositional area (Keefer and Johnson, 1983). Topographically, earthflows are commonly found on hillslopes with low planform curvature (Ohlmacher, 2007).

Active earthflows exhibit seasonal movement patterns primarily governed by precipitation and groundwater levels, and they can require several weeks of cumulative rainfall before the onset of movement (Kelsey, 1978; Iverson and Major, 1987). Earthflows can potentially dominate sediment delivery to channels in erosive landscapes (Putnam and Sharp, 1940; Swanson and Swanson, 1977; Kelsey, 1978), and yet they seldom fail catastrophically (Iverson, 2005). We specifically distinguish earthflows from large-displacement, catastrophic single-event failures, such as rockslides, translational bedrock slides, debris flows, and rotational slumps (Cruden and Varnes, 1996).

[†]Present address: Division of Geological and Planetary Sciences, California Institute of Technology, 1200 E. California Blvd., Pasadena, California 91125, USA.

E-mail: bmackey@caltech.edu

Extensive work has been undertaken on the behavior of individual earthflows at the daily and seasonal scales (e.g., Iverson and Major, 1987; Malet et al., 2002; Coe et al., 2003; Schulz et al., 2009a). Other research foci include specific earthflow mechanics such as shear zone dilatancy and strengthening (Iverson, 2005; Schulz et al., 2009b) and the evolution of earthflow material strength over time (Maquaire et al., 2003). Many attempts have been made to model earthflow mechanics and rheology (e.g., Brückl and Sehdegger, 1973; Craig, 1981; Savage and Chleborad, 1982; Iverson, 1986c; Vulliet and Hutter, 1988; Baum et al., 1993; Angeli et al., 1996; Savage and Wasowski, 2006; van Asch et al., 2007), primarily to describe or replicate the observed behavior of specific earthflows.

Earthflow Spatial Patterns and Sediment Yield

To assess the contribution of landsliding to regional erosion rates, we must quantify the transfer of sediment from slope failures to active channels and compare this sediment yield to catchment-wide erosion data sets, such as suspended sediment records. Complicating this task, slope failures vary in timing, location, size, mechanism, postfailure behavior, and the efficacy of sediment delivery to the channels (Benda and Dunne, 1997; Lave and Burbank, 2004; Korup et al., 2010). Some types of landslides (e.g., debris slides and translational landslides) can deliver all the failed mass to channels shortly after failure, and such behavior is amenable to approximating landslide-derived erosion rates by magnitude-frequency statistics of landslide areas and volumes (e.g., Hovius et al., 1997; Lave and Burbank, 2004; Stark and Guzzetti, 2009; Larsen et al., 2010). In contrast, individual earthflows can continue moving and actively supplying sediment to a channel for hundreds of years (Bovis and Jones, 1992), so the rate of sediment flux at the earthflow-channel interface is more pertinent to sediment yield than earthflow size or volume.

To assess the contribution of earthflow movement to regional erosion rates, earthflow velocities and sediment yields must be accurately mapped and averaged over sufficiently large temporal and spatial scales. This helps to ensure that estimates of earthflow-generated sediment yield are not biased by variations in decadal-scale climate (Bovis and Jones, 1992; Mackey et al., 2009), or dominated by a peak in activity (e.g., a surge) from an individual earthflow (Kelsey, 1978). In sharp contrast to the many data sets of catastrophic landslides (e.g., Malamud et al., 2004a), long-term, regional-scale inventories of slow-moving landslides are scarce (cf. Kelsey,

1978; Keefer and Johnson, 1983; Bovis and Jones, 1992; Ohlmacher, 2007). Accurate inventories of regional earthflow activity will enable us to quantify rates of earthflow-generated sediment yield and identify spatial patterns of slide activity that influence long-term movement.

Long-Term Earthflow Evolution

When observing an earthflow-prone landscape, especially on high-resolution digital topography (Fig. 1), a striking feature is that nearly all hillslopes appear to have been affected by mass movement, and the morphology of earthflow and landslide activity is widespread (Putnam and Sharp, 1940). Multiple generations of dormant slope failures appear to surround the comparatively small fraction of active terrain. This observation has prompted speculation that longer-term external forcing may modulate earthflow activity, such that many of the dormant slope failures we see in the landscape today are an artifact of past periods of activity. Sources of external forcing include glacial-interglacial or shorter-term variations in climate (e.g., Bovis and Jones, 1992; Fuller et al., 2009), episodes of base-level fall (Palmquist and Bible, 1980), earthquakes (Lawson, 1908; Keefer, 1984), or land use (Kelsey, 1978).

Although the seasonal behavior of individual earthflows has been well documented,

we lack conceptual models describing the long-term evolution of an earthflow-prone landscape, and even the long-term evolution of an individual earthflow. For clay-rich, earthflow-prone hillslopes (Fig. 1), there is nothing comparable to the colluvial hollow and debris-flow framework applicable to soil-mantled uplands (Dietrich and Dunne, 1978; Lehre and Carver, 1985), or the competing soil creep and fluvial erosion processes applicable to gentle ridge and valley topography (Perron et al., 2009).

In an attempt to address this knowledge gap, we here propose a largely unexplored alternative to theories of long-term external forcing. Earthflow activity may be dependent on factors intrinsic to individual earthflows, namely, the long-term balance of soil and rock entering and leaving the earthflow. The rate of material leaving the earthflow via mass translation and fluvial erosion is unsustainably fast over long time periods (Mackey et al., 2009), whereas the supply of readily mobilized earthflow colluvium is limited by rates of bedrock weathering and expansion of the earthflow source zone. The imbalance of material entering and exiting the earthflow can only be reconciled with brief periods of earthflow activity, separated by long periods of dormancy, to allow time for mass to accumulate via weathering and recharge the earthflow source zone.

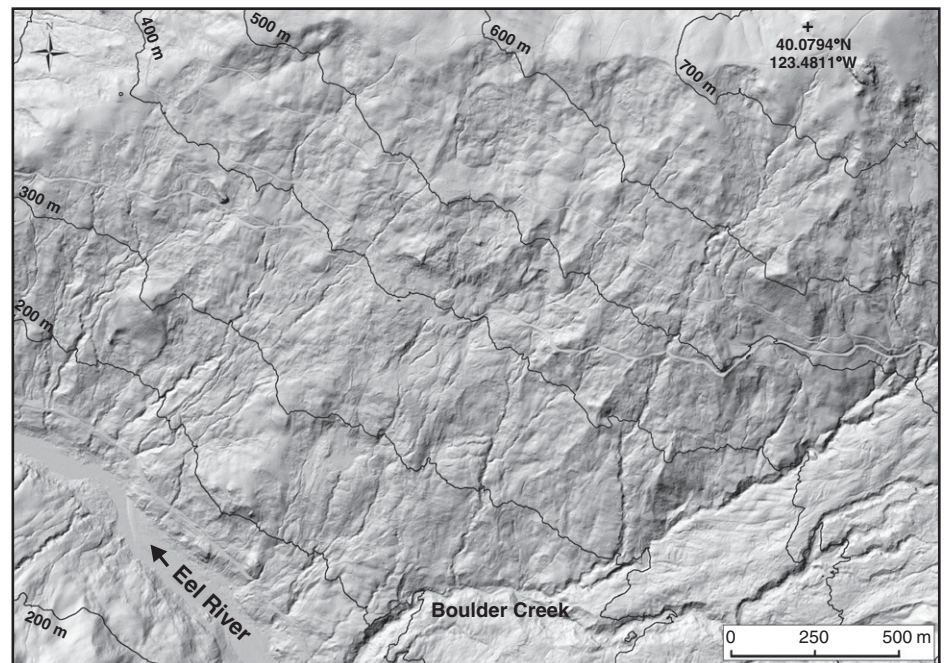


Figure 1. Shaded relief image of light detection and ranging (LiDAR)-derived digital topography of earthflow-prone hillslope along the Eel River, California. Trees have been filtered from the LiDAR data, leaving the bare earth. This hillslope has multiple generations of earthflow activity with a range of sizes and failure styles.

Active Earthflow Characteristics, Sediment Yield, and Landscape Evolution

To assess the contribution of earthflows to regional sediment yield, and their control of landscape form, we investigated some variables that control sediment flux in earthflow terrain. These variables provide a basis for quantifying regional earthflow erosion at geomorphically significant time scales. We asked four basic questions: (1) how much of the terrain is active, (2) do active earthflows have characteristic spatial attributes such as slope, lithology, aspect, planform shape, probability distribution as a function of area, position on the hillslope, or connectivity to major channels, (3) what proportion of the suspended sediment load in a channel network is attributable to earthflow mass movement, and (4) can we combine remote-sensing data and field observations to develop a conceptual framework for the evolution of earthflow terrain?

To address these questions, we focused on the Eel River catchment in northern California (Fig. 2), where the combination of weak mélangé rock, active tectonics, and high rates of seasonal rainfall leaves the watershed especially prone to slope instability. The 9450 km² Eel River has the highest sediment yield (2200 t km⁻² yr⁻¹) of any nonglacial river of its size in the contiguous United States (Brown and Ritter, 1971; Wheatcroft and Sommerfield, 2005) and is an ideal location to study active earthflow processes. We generated detailed, regional-scale maps of active earthflows underpinned by airborne LiDAR, historical aerial photography, and field inspection. We describe the challenges of accurately mapping active movement in inherently unstable terrain, and outline methods we developed to objectively map active earthflows in this landscape.

REGIONAL STUDY AREA—EEL RIVER, NORTHERN CALIFORNIA

Lithology and Tectonics

The northern California Coast Ranges are composed of the Franciscan Complex, a penetratively sheared set of metasedimentary rocks that represents a Jurassic–Cretaceous accretionary prism. The Franciscan Complex consists of three structurally separated belts, the Eastern, Central, and Coastal belts, reflecting the cumulative accretion of oceanic sediments to western North America (Jayko et al., 1989; McLaughlin et al., 2000). The Central belt is especially prone to landsliding. It runs through much of the Eel River catchment and consists of an extensive Late Jurassic to Middle Cretaceous argillaceous mélangé matrix, encompassing blocks and slabs of sandstone

and shale turbidite sequences (McLaughlin et al., 2000). During oblique dextral translation, large blocks of older, metasandstone, metabasalt, and blueschist-grade rocks were incorporated into the penetratively sheared matrix of the Central belt from the older eastern units. These more competent blocks have a significant local influence on the topography, persisting as erosion-resistant topographic highs amid the mélangé (Fig. 3). The northwest-trending structural grain strongly influences the modern topography, with major axial drainages and ridges trending northwest (McLaughlin et al., 1982).

The postemplacement tectonic history of northern California Coast Ranges has been dominated by the northerly migration of the Mendocino triple junction (MTJ) since the Miocene. The Pacific and Gorda plates are translating north relative to North America along the Cascadia megathrust, creating the San Andreas fault to the south (Furlong and Schwartz, 2004). This generates two zones of uplift that migrate

north at ~5 cm/yr (Furlong and Govers, 1999) and have a profound influence on the landscape, causing river capture and drainage reversals (Lock et al., 2006). A series of northwest-trending emergent fault systems cut through the northern California Coast Ranges associated with the advance of the Mendocino triple junction (Kelsey and Carver, 1988).

Uplift Rates, Erosion, and Geomorphology

Due to active tectonics, weak rocks, and high rates of erosion, many geomorphic studies have focused on the Eel River watershed. Localized rock uplift rates along the northern California coast approach 5 mm/yr near Cape Mendocino (Merritts and Bull, 1989) (Fig. 2), although these rapid rates appear to be related to uplift of the coastal King Range (Dumitru, 1991) and likely do not project inland.

Several approaches have been used to constrain background levels of rock uplift and erosion in the

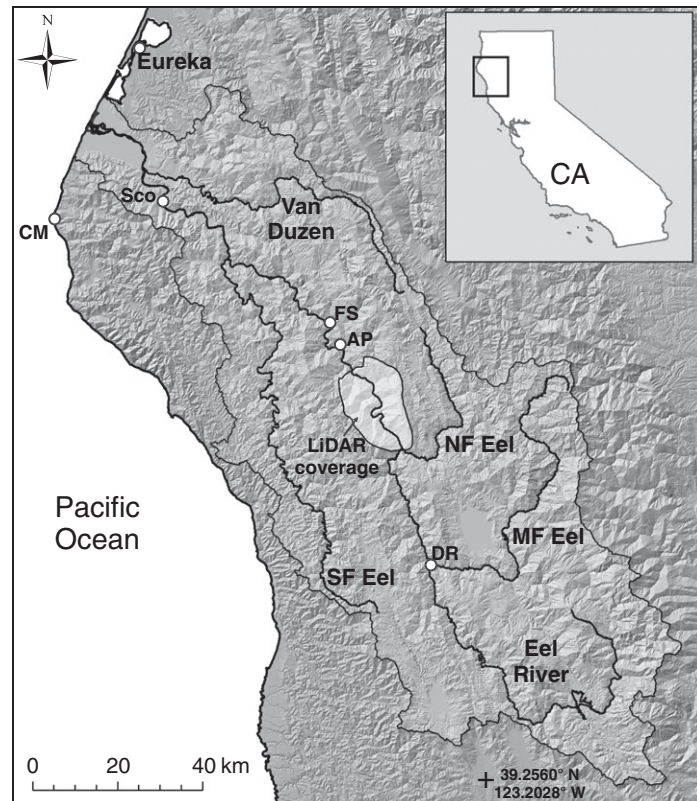


Figure 2. Eel River catchment and location of the study area along main stem Eel River, northern California. Light detection and ranging (LiDAR) data were acquired over the 230 km² region shaded in white. Branches of the Eel River include Middle Fork (MF), North Fork (NF), and South Fork (SF). Locations mentioned in text: Alderpoint (AP), Dos Rios (DR), Fort Steward (FS), Scotia (Sco), Cape Mendocino (CM). Note the strong northwest-trending structural grain visible in the shaded relief background map.

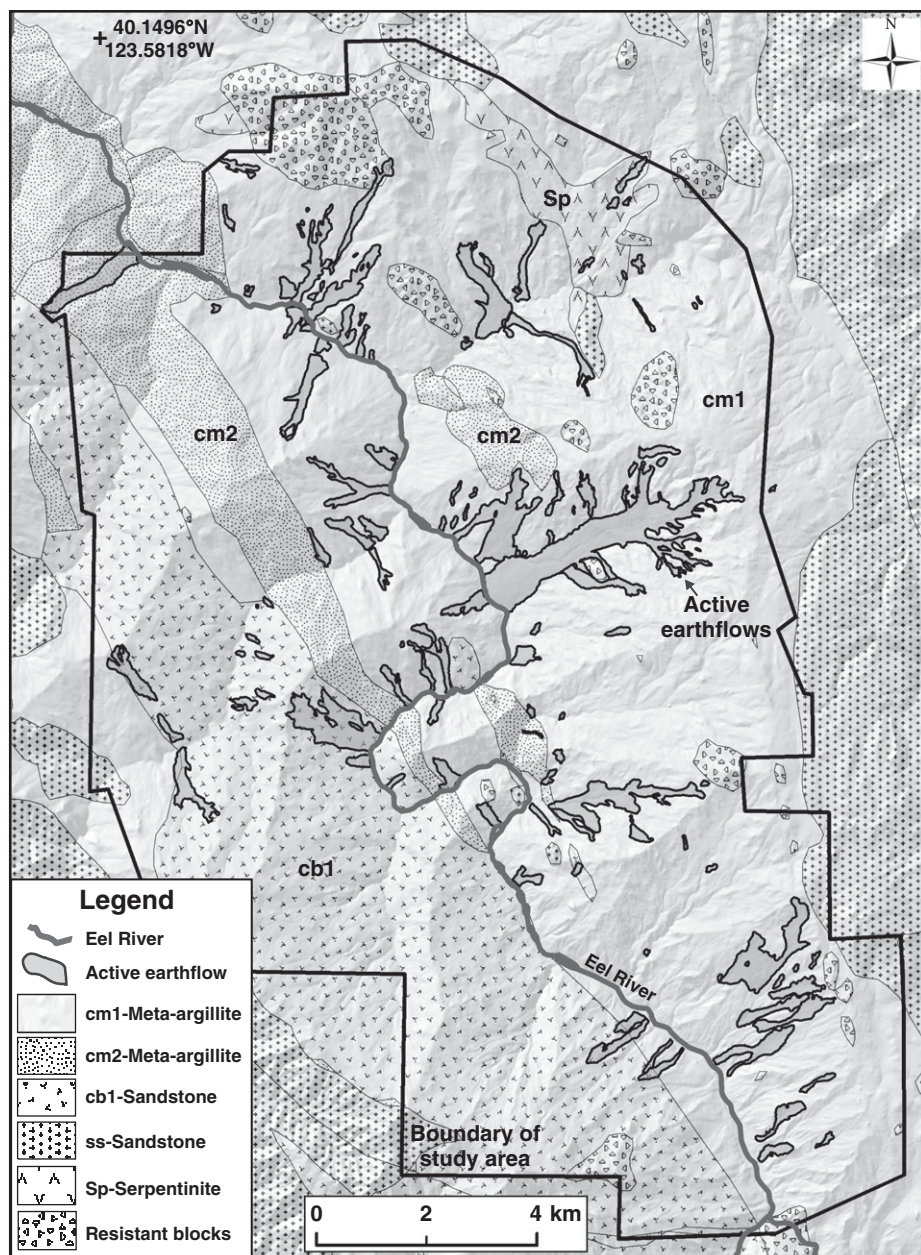


Figure 3. Simplified lithological map modified from Jayko et al. (1989) and McLaughlin et al. (2000) overlying a shaded relief map. See Table 1 for detailed descriptions. Active earthflows are superimposed on the lithology.

inland portion of the Eel River catchment. Fuller et al. (2009) used cosmogenic isotope measurements and optically stimulated luminescence dating to calculate late Pleistocene–Holocene erosion rates for the upper South Fork Eel River (Fig. 2) of ~ 0.3 mm/yr (~ 750 t km⁻² yr⁻¹ assuming bedrock density $\rho = 2.5$ g/cm³). Most relevant to the time scale and focus of our study, Wheatcroft and Sommerfield (2005) reanalyzed suspended sediment data (1950–2000) collected at Scotia (Fig. 2) and calculated an average suspended sediment yield of 2200 t km⁻² yr⁻¹ across 8063 km² of the Eel

River catchment. This sediment yield equates to a catchment-averaged bedrock erosion rate of ~ 0.9 mm/yr, and we adopt this as representative of modern erosion rates. This period includes both anthropogenic effects (e.g., grazing, forestry) and midcentury storms (Brown and Ritter, 1971; Sloan et al., 2001; Sommerfield et al., 2002; Sommerfield and Wheatcroft, 2007). Bed load is poorly constrained but decreases downstream as the weak rocks disaggregate, and it is significantly less than suspended load at the Scotia gauging station (Brown and Ritter, 1971; Lisle, 1990).

Hillslope geomorphology within the Eel River watershed is well described by Kelsey (1980) and Muhs et al. (1987), who highlighted the roles of contrasting geomorphic processes operating in different rock types. Topography is generally described as either “hard” or “soft,” depending on its morphology and resistance to mass wasting. The harder, competent, steep sandstone rocks in the Franciscan Complex feature well-organized ridge and valley drainage networks, with erosion dominated by fluvial and debris-flow incision (e.g., Stock and Dietrich, 2006), and local relief can exceed 1000 m. Toe-slope failures, known as debris slides, are also common in harder rocks (Kelsey, 1980; Kelsey et al., 1995). In contrast, the weaker, fine-grained mélangé units (soft topography) have a dense but poorly developed drainage network, and longer low-gradient slopes (30–35%), and erosion is dominated by earthflows and ephemeral gullies (Fig. 1). The most comprehensive study of earthflow processes in the Eel River catchment was undertaken by Kelsey (1977, 1978, 1980) in the Van Duzen river watershed, a large tributary of the Eel River at the northern end of the drainage basin (Fig. 2). Although comprising just 1% of the Van Duzen watershed area, earthflows contributed 10% of sediment to the channel.

Main Stem Eel River Study Site

This study focuses on a remote section of the main stem Eel River between Dos Rios and Alderpoint (Fig. 2). Brown and Ritter (1971) noted that this site has one of the highest concentrations of earthflow activity and sediment yield in the Eel River catchment and advocated further studies of sediment production in this location. Lithology in this area is predominantly the argillaceous mélangé of the Central belt Franciscan Complex (Fig. 3), characterized by long, low-gradient slopes and extensive slope instability (Fig. 1). The argillaceous mélangé is not conducive to conifer growth and was open oak grassland at the time of European settlement in the 1850s. This attracted ranchers (Carranco and Beard, 1981), and the primary land use remains low-density cattle ranching. Conifer growth and forestry are generally limited to isolated sandstone outcrops. Rainfall measured at Alderpoint averages 1.3 m/yr, and it falls primarily between October and April.

Slope failures in the study area range from small slumps to huge earthflow complexes (Brown and Ritter, 1971; Mackey et al., 2009; Roering et al., 2009). On a single hillslope, earthflows often exhibit complex crosscutting and nested relationships and span a range of size, age, activity state, and failure style (Fig. 1). Descriptions of the large landslides and earthflows along the Eel River canyon between Dos Rios and

Alderpoint were initially confined to engineering reports by the California Department of Water Resources (Dwyer et al., 1971; Scott, 1973; Smith et al., 1974). More recently, Mackey et al. (2009) studied an earthflow on Kekawaka Creek, a tributary to the Eel River. They highlighted the steady decline in earthflow velocity since the 1970s and determined long-term movement rates by measuring meteoric ^{10}Be accumulated in the earthflow soil. Roering et al. (2009) used satellite-based Interferometric Synthetic Aperture Radar (InSAR) to monitor seasonal movement of the Boulder Creek landslide, and estimated a minimum erosion rate of 1.5 mm/yr ($\sim 3400 \text{ t km}^{-2} \text{ yr}^{-1}$) across the earthflow source area.

Very little data exist on the depth of large landslides and earthflows along the Eel River. The exceptions are two landslides in the lower reaches of the Middle Fork Eel River (California Department of Water Resources, 1970), $\sim 34 \text{ km}$ southeast of our study area (Fig. 2), but in comparable Central belt Franciscan rock. Boreholes in the 1.6-km-long, 0.45 km^2 Salt Creek landslide, 3.5 km upstream of Dos Rios, revealed a landslide thickness of 33–35 m toward the toe. The larger, 1-km-long, 0.64 km^2 Salmon Creek landslide is 16 km upstream from Dos Rios, and a drill hole in this landslide was sheared off at 34 m.

METHODS—OBJECTIVELY MAPPING EARTHFLOW ACTIVITY WITH HIGH-RESOLUTION TOPOGRAPHIC ANALYSIS AND PHOTOGRAMMETRY

Background—Landslide Mapping

Landslide mapping has traditionally been undertaken by a combination of stereo-pair aerial photo and topographic map analysis, in concert with field verification. Aerial photo analysis can efficiently cover a large area, but at the expense of accuracy, especially in forested terrain, and problems arise in accurately relocating features on a photograph to the base topographic map (Malamud et al., 2004a). Field mapping yields greater accuracy (especially with modern global positioning system [GPS] technology), but at the expense of high labor costs and the limited extent of terrain that can be covered (Wills and McCrink, 2002; Haneberg et al., 2009). In recent years, satellite-based InSAR mapping has proven to be effective in locating slow, sustained mass movement (e.g., Hilley et al., 2004). Roering et al. (2009) successfully identified active earthflows in the Eel River catchment using data from the L-band PALSAR ALOS satellite, although this record only extends back to 2006.

The increasing availability of high-resolution topography acquired through airborne laser swath mapping (LiDAR) has greatly enhanced

the ability of researchers and practitioners to map mass-movement features across a broad area. LiDAR-based mapping allows greater accuracy in both correct feature identification and location than is available with traditional aerial photo and field mapping approaches.

Although LiDAR maps have been a great improvement on previous approaches (Schulz, 2007), confidently mapping active movement in terrain with multiple episodes of deep-seated failure can be a subjective exercise (Van Den Eeckhaut et al., 2005, 2007). In landscapes prone to pervasive slope instability with multiple generations of landsliding, distinguishing between active and dormant mass movement is difficult without additional information on feature activity (e.g., Fig. 1).

Some qualitative estimates of earthflow activity state or age can be made from landslide morphology (McKean and Roering, 2004; Booth et al., 2009). Over time, morphological features attributable to landslide or earthflow movement (e.g., sharp headscarps, tension cracks, compressional folding, and lateral margins) become smoothed out and attenuated by small-scale surficial or diffusive processes (e.g., soil creep, bioturbation) when a landslide stops moving (Wieczorek, 1984; González-Díez et al., 1999). Figure 4 shows earthflows adjacent to the Eel River that qualitatively appear to span a range of activity states. Two currently active features with fresh kinematic structures (such as lateral levees and advancing lobes) adjoin a dormant landslide, where much of the small-scale morphology has been erased, leaving subtle headscarps and lateral margins. The older landslide has been deeply dissected by an axial gully, which is typical of many dormant earthflows.

Acquisition of Airborne LiDAR

The National Center for Airborne Laser Mapping (NCALM) acquired a high-resolution (1 m) LiDAR data set of the 230 km^2 study area in September 2006 (Fig. 2). The raw data were processed by NCALM and converted to digital elevation models (DEMs). The elevation grids included both unfiltered elevation (data include tree and building elevations, Fig. 5) and filtered or “bare earth” elevation models from which vegetation and structures had been removed (Fig. 1) (Carter et al., 2007; Slatton et al., 2007). From the bare earth LiDAR data, we extracted statistics of regional slope and aspect.

Historical Aerial Photo Orthorectification

The earliest extensive aerial photo set covering our field area in the Eel River catchment was flown in 1944 (U.S. Forest Service DDD series). These 1:24,000 scale photos are of high quality; trees, buildings, and subtle topographic features are readily identifiable. We acquired medium resolution ($30 \mu\text{m}$) scans of 18 photos to provide coverage of the study area.

For quantitative analysis, aerial photographs must be referenced to the ground and orthorectified to remove lens distortions and topographic effects (Wolf and Dewitt, 2000). This requires the calibrated focal length of the lens, the coordinates of fiducial markers on the edge of the photo, a digital elevation model of the terrain, and ground-control points (GCPs) to collocate features on the photo with features on the ground. For GCPs, we identified features such as small trees, buildings, or isolated rock outcrops on unequivocally stable terrain (such as ridges and terraces) and collocated the identical

Figure 4. Active versus dormant earthflow morphology. Two active earthflows show sharp morphological features, whereas a large dormant earthflow to the south has had much of the finer-scale morphology attenuated by surficial processes. The northern active earthflow propagated downslope from 1952 to 1966. The abandoned Northern Pacific Railroad runs along the southwest side of the Eel River.

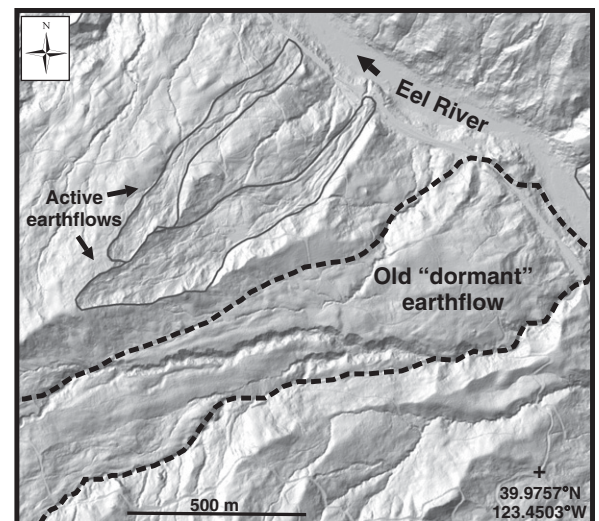
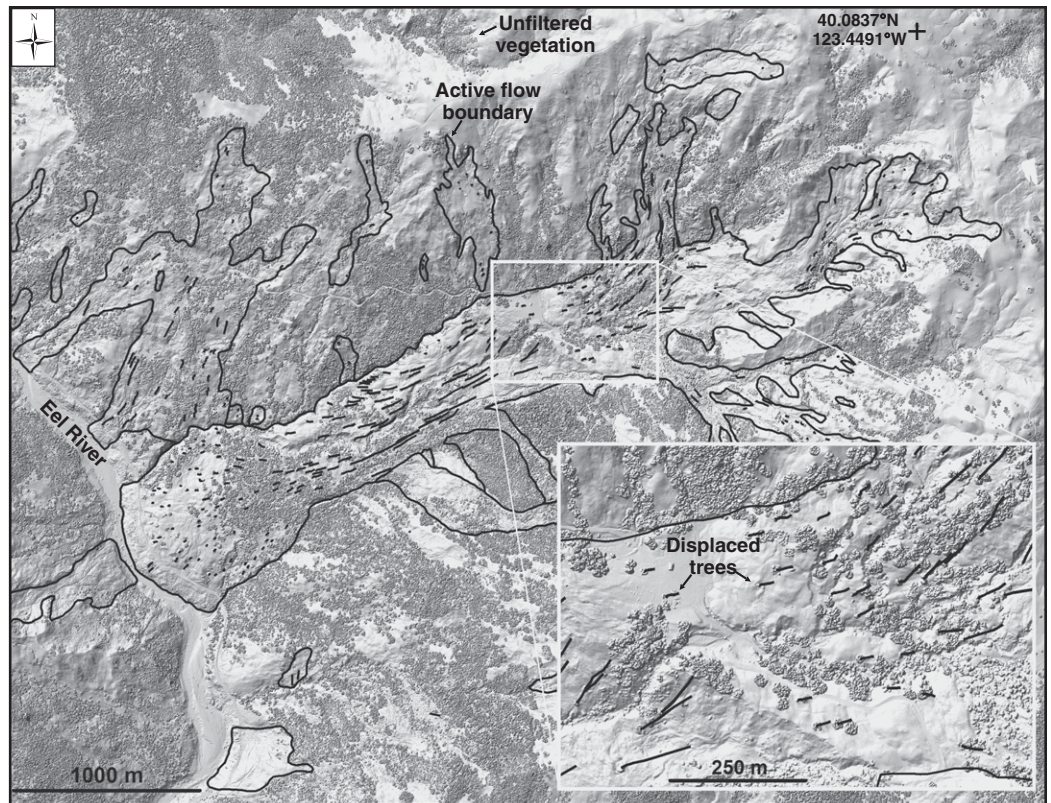


Figure 5. Unfiltered shaded relief map of the Boulder Creek earthflow showing tree displacement vectors depicting earthflow movement. Margins of active earthflows and individual tree displacements are shown in black. Inset shows displacement at the midsection of the flow, where it crosses a structural barrier running obliquely across the transport zone. Note the large toe advancing from the northeast. Eel River runs south to north along the toe of the Boulder Creek earthflow.



features on both the unfiltered LiDAR shaded relief image and the photo.

We were not able to locate camera information or calibration reports for the 1944 series of photos, but an estimated focal length (210 mm) from a database of typical camera specifications (Slama, 1980) achieved a median rectification error of ~ 2.3 m. We used image-processing software to measure the coordinates of fiducial marks around the margins of the photos on true-scale scanned photos and assumed a perfect principal point of focus ($x, y = 0, 0$) to construct the photo coordinate system. We used the 1 m^2 LiDAR bare earth elevation as the elevation model and the unfiltered 1 m^2 LiDAR slope and shaded relief maps as reference images to rectify the photographs within ERDAS Imagine 9.3 software.

Through this process, we could rectify the photos with a high degree of accuracy, and relocate features on the photos as they were placed on the ground in 1944. We compared the position of stable features on the LiDAR with the rectified photos across the study site in order to estimate orthorectification error.

Estimating Earthflow Movement

The earthflows of the Eel River catchment commonly have isolated oak trees and bushes growing on the earthflow surface (Fig. 5). These

trees often continue to grow on the landslide mass as it translates downhill and are readily identifiable in photographs, on unfiltered LiDAR maps, and in the field. By comparing differences between the 1944 photos and the unfiltered LiDAR data acquired in 2006, we were able to track the locations of individual trees and construct slope-corrected displacement vectors for the 62 yr time interval. We used this approach to objectively map historically active earthflows and discriminate between stable and moving terrain.

The distribution of trees varies across the study area and between different earthflows. Some earthflows have many long-lived trees that can be used to construct a detailed vector field of displacement (Fig. 5). On other earthflows, trees can be sparse, and the extent of movement is more difficult to objectively discern with tree displacement vectors alone. To delineate the margins of earthflows, we used an iterative approach, carefully comparing the rectified 1944 photos and the LiDAR imagery. The primary guide to mapping an earthflow margin was the boundary between stable and moving trees. The margins of active earthflows typically feature a subtle morphological structure, such as a headscarp, lateral levee or pressure ridge, or a toe-lobe thrust, and we used these morphological features to guide the fine-scale margin delineation

between active and stable trees. In some areas with few or no trees suitable for quantifying displacement, we were able to detect movement based on changing earthflow morphology. For example, advancing toes or headscarp retrogression can be readily identified by comparing the photos with the LiDAR maps. We took a conservative approach to mapping: if we could not confidently map either vegetation displacement or morphological change, we did not include the terrain as an active earthflow. Some earthflows, such as the Mile 201 slide, underwent extensive landscaping work to protect a railway that runs adjacent the river. As trees and features on these earthflows had been altered by heavy machinery, we relied on engineering reports (e.g., Scott, 1973) to estimate total displacement. Where we mapped isolated displacements in different parts of an earthflow, we amalgamated these into one larger contiguous feature when justified by morphology. Additionally, we distinguished stable patches within a larger earthflow from the neighboring mobile terrain.

We visited earthflow features in the field over four field seasons to confirm the reliability of our technique. On the ground, active earthflows exhibit fresh headscarps, exposed “mole-track” lateral margins with slickensides (Fig. 6A), disturbed, densely cracked hummocky terrain (Kelsey, 1978; Keefer and Johnson, 1983), fresh

extensional cracks, and occasionally trees that have been stressed, toppled, or killed by intense ground deformation (Fig. 6B). Conversely, stable or dormant earthflows, while retaining much of the hummocky terrain and characteristic macroscale earthflow morphology, do not exhibit the same degree of fresh ground disturbance (Fig. 4).

We mapped earthflow features as detailed polygons using ESRI ArcMap 9.2 software and constructed a statistical database of the individual earthflows. By combining LiDAR, rectified photos, and field inspection, we objectively mapped landslide displacement (≥ 5 m) over the 62 yr interval across the 226 km² study area.

Earthflow Sediment Production

During winter, the earthflows push out into the channels, and erosion of the toe occurs by slumping from the toe face. Fine sediment (clay, silt, and fine sand) is carried off in suspension during high flows (Brown and Ritter, 1971), and coarse sand and gravel accumulates as bed load in the channel. Earthflows can also transport large boulders (up to 15 m diameter), which are pushed into the channel, and which can armor the bed while they slowly weather and disintegrate in place, frequently creating knickpoints on the stream profile (Kelsey, 1978). These large boulders are estimated to contribute less than 2% of the earthflow volume, with 90% of the earthflow colluvium finer than 76 mm in diameter (Smith et al., 1974). Much of the argillaceous rock rapidly disaggregates when subjected to fluvial erosion and wetting and drying processes in the channel and becomes suspended load. In calculating sediment production from earthflows, we distinguished earthflows that discharge sediment directly into a channel or major gully from flows that are disconnected from the channel network and do not represent active sediment sources. We only included the earthflows connected to channels when calculating earthflow sediment production.

Landslide volumes and their contribution to sediment yield can potentially be estimated from the planform area (Hovius et al., 1997; Lave and Burbank, 2004; Malamud et al., 2004a). Given sparse constraints on earthflow depths, and the small fraction of total earthflow volume that enters the channel network in any given year, we focused on the depth and velocity of material at the earthflow toe.

We have no direct data as to the depth to the failure surface in our study area (e.g., from drill holes), but approximations can be made by calculating the toe height at the channel interface (Kelsey, 1978). We used the depth data from the Middle Fork Eel River earthflows (California

Department of Water Resources, 1970) to guide depth estimates of the larger features in our study area. Because velocities can vary across an earthflow toe due to differential movement, where possible we averaged multiple measurements of tree displacement to obtain representative earthflow toe velocities. To calculate the annual sediment delivery attributable to earthflow movement into a channel, we multiplied the average annual toe velocity (from the 62 yr photo-LiDAR-derived vectors) by the width and depth of the earthflow toe (Fig. 7). Based on repeat measurements, we assigned uncertainties of 25% for the depth, 10% for the width, and 10% for the velocity when calculating sediment flux from each individual earthflow. To convert to

a sediment yield (metric t km⁻² yr⁻¹), we assume a density of earthflow colluvium of 2.1 ± 0.1 g/cm³ (Kelsey, 1978; Mackey et al., 2009).

One limitation with this approach is the potential for surface velocities to represent a maximum rate, rather than a depth-averaged flow velocity, owing to deformation within the earthflow mass. Although the term “earthflow” implies significant internal deformation, field data for earthflows similar to those in our study site emphasize that the predominant mechanism is sliding or plug flow, and most deformation (>75%) is accommodated in a narrow basal layer (Keefer and Johnson, 1983; Vulliet and Hutter, 1988; Zhang et al., 1991a; Swanston et al., 1995; Savage and Wasowski, 2006; Glastonbury and Fell, 2008).

Figure 6. Field evidence for earthflow activity. (A) Lateral margin of an active earthflow showing slickenlines. (B) View up the active Penstock earthflow showing the disturbed ground and distressed trees. Shrubs in foreground are ~1 m tall.

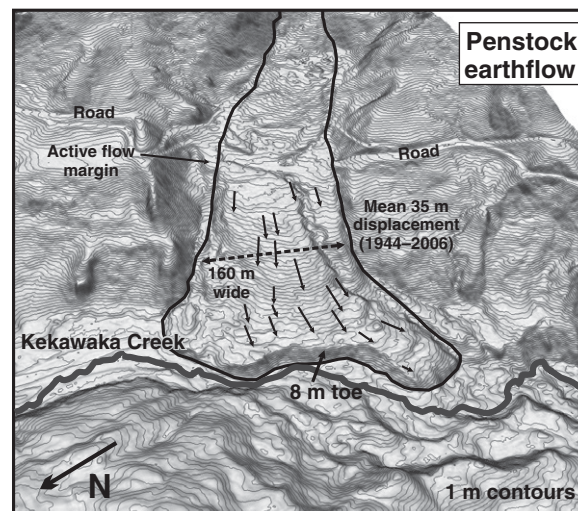
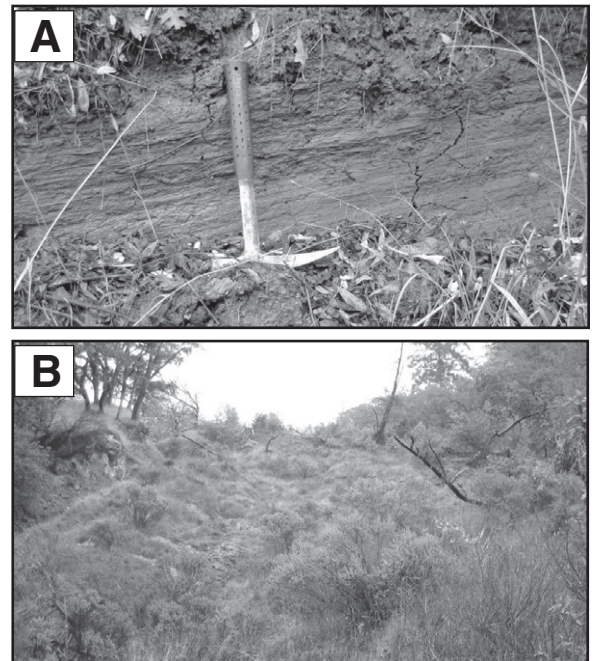


Figure 7. Oblique view of the Penstock earthflow looking southeast across Kekawaka Creek, illustrating the measurements taken to estimate annual sediment flux from each earthflow. Center of earthflow toe is 40.1032° N, 123.4940° W.

If, for simplicity, we assume a Newtonian deformation profile, and that sliding accounts for 75% of movement (leaving 25% for internal deformation), then we are potentially overestimating mass flux by 10% when not accounting for internal deformation. Since the depth behavior of earthflows in our study site is unconstrained, we do not explicitly include this in our calculations of sediment delivery to channels. Rather, we note that we are potentially overestimating sediment delivery by ~10% if internal deformation is 25% of the total movement. Drag from earthflow margins does not appear to have a major effect on the planform velocity profile. Lateral strain is primarily taken up by fault-like longitudinal structures on the margins or within the earthflow body (Fig. 5) (Schulz et al., 2009b). By taking the average measurements of multiple trees on the toe, we minimize errors from variations in planform velocity.

RESULTS

Spatial Distribution of Earthflows

Across our study area along the Eel River, we identified 122 earthflow features that moved during the interval 1944–2006 (Fig. 8). Over the study area of 226 km², we mapped active earthflows covering 16.5 km², indicating 7.3% of terrain moved between 1944 and 2006. We note this to be a minimum estimate, since it is possible for earthflows with less than 5 m of cumulative displacement to be active, but below our level of detection, or for earthflows without trees or notable surface deformation to have gone undetected. Table DR1 documents the spatial attributes of the individual earthflows.¹

Earthflow Displacements

In total, we tracked displacements of 998 features (trees, shrubs, or rocks) distributed across the 122 earthflows (with an average density of one displaced feature in every 17,000 m² of earthflow terrain), shown on Figure 8. The distribution of displacements is positively skewed, with a median displacement of 23.9 m, and an interquartile range (middle 50%) of 14.6–42.3 m (Fig. 9A). The maximum displacement was 175 m, recorded on the Boulder Creek earthflow (Fig. 5). Over the 62 yr interval, the median earthflow velocity across all moving features

was 0.4 (0.2–0.7) m/yr (median and interquartile range). By comparing the locations of stable features both on the photos and in the LiDAR data, we estimated the error associated with photo rectification. Rectification error was small in comparison to the tree displacement, with a median error of 2.3 (1.3–3.2) m (Fig. 9B).

Earthflow Shape and Area

The planform shapes of individual earthflows vary greatly and can diverge significantly from the classical hourglass planform. Many earthflows have complex and intricate margins, whereby multiple small tributary earthflows feed into a centralized transport zone (Figs. 5 and 8). Earthflows can bifurcate around resistant topography, lower ridges, and capture the drainage area of adjacent terrain. In several cases, stable regions persisted within an earthflow complex (Fig. 8). The 122 earthflows have a median area of 36,500 m² and interquartile range of 12,500–117,000 m². The largest active earthflow in the study site, the Boulder Creek earthflow (3.1 km²; Fig. 5), is over 3 times the area of the next largest feature (0.94 km²), the Island Mountain earthflow (Fig. 8). The larger earthflows dominate small (<3 km²), scallop-like tributary catchments, which typically have low planform curvature, and could be described as “earthflow basins.” The Boulder Creek earthflow is the dominant feature in the ~15 km² Boulder Creek catchment.

The probability distribution of earthflow areas (Fig. 10) has a highly positive skew and is well described by a lognormal distribution with parameter values of $\mu = 10.65 \pm 0.27$ and $\sigma = 1.51 \pm 0.17$ (95% confidence bounds). The tails of many landslide area distributions are recognized to show power-law behavior, with frequency decreasing as the inverse power of area. The tail of the earthflow distribution, where area exceeds 80,000 m², can be approximated by a power law with an exponent of -1.06 (Fig. 10).

There is a statistically different change in the aspect ratio of earthflows as they increase in area. Earthflows with planform areas less than 80,000 m² have an average aspect ratio (averaged length/width) of 4.5 ± 3.1 (mean \pm standard deviation) (Fig. 11A). In comparison, when earthflow area exceeds 80,000 m², the aspect ratio is significantly different at 7.2 ± 3.9 (Fig. 11B), indicating that larger earthflows tend to be more elongate (Fig. 11C).

Of the larger earthflows, 25 extend from the channel up to a ridgeline or major break in slope at the scale of the hillslope lengths (1–3 km). Among the 97 earthflows that do not span from channel to ridge top at this scale, 37 have a prominent interface with a major channel (Eel

River or major tributary), whereas 60 are located higher on hillslopes and do not discharge into large channels (Table DR1 [see footnote 1]). This characterization is distinct from our previous method of documenting earthflows that constitute active sediment sources (described in section 3.5, “Earthflow Sediment Production”). In that classification, some earthflows positioned high on slopes are bisected by or feed into large gullies and thus indirectly supply sediment to the primary fluvial network, but do not span ridgetop to channels.

Slope and Lithology

We calculated the longitudinal slope of each earthflow (headscarp-to-toe elevation range/centerline length), in addition to the average slope of all 4 m LiDAR DEM pixels (16 m²) within each earthflow polygon (Fig. 12; Table DR1 [see footnote 1]). To compare earthflow topography to the distribution of regional slopes, we calculated the slope of all 4 m pixels in the study area.

The longitudinal earthflow slope distribution (Fig. 12A) has an approximate normal distribution with a mean value of $31\% \pm 7\%$ (mean \pm standard deviation). Larger earthflows are generally less steep (Fig. 12B); specifically, no earthflows with an area over 250,000 m² have longitudinal slopes exceeding 30%.

We compared normalized distributions of 4 m slope pixels for the entire study area, and the 16.5 km² of active earthflows, respectively (Fig. 12C). The distributions are statistically different based on an F-test ($\alpha = 0.05$), but mean values are very close at 34% for earthflows and 36% for all terrain. The study area has a greater fraction of steeper terrain, as shown by a more positively skewed distribution than the earthflows (Fig. 12C).

Of the 122 mapped active earthflows, 98 (82% of the active earthflow area) occur in the penetratively sheared mélange unit (cm1) (Fig. 3; Table 1).

Earthflow Aspect

Kelsey (1978) noted that earthflows along the Van Duzen River tend to have a southerly aspect. To test whether active earthflows along our Eel River study site have a preferential aspect, we calculated the median aspect of 4 m DEM pixels within each earthflow polygon (Fig. 13A). The mean earthflow aspect is 210°, with a mean resultant vector of 0.42. Applying Rayleigh's test for significance of a mean direction, for this data set, the critical resultant vector ($\alpha = 0.05$, $n > 100$) is 0.17, indicating that the 122 earthflows have a significant mean southwesterly aspect.

¹GSA Data Repository item 2011099, Table DR1, a .xls file that documents the spatial characteristics and movement of the earthflows, and Figures DR1–DR2, which illustrate the stages of earthflow evolution described in Figure 14 with field examples, is available at <http://www.geosociety.org/pubs/ft2011.htm> or by request to editing@geosociety.org.

Earthflow activity and erosion, Eel River, California

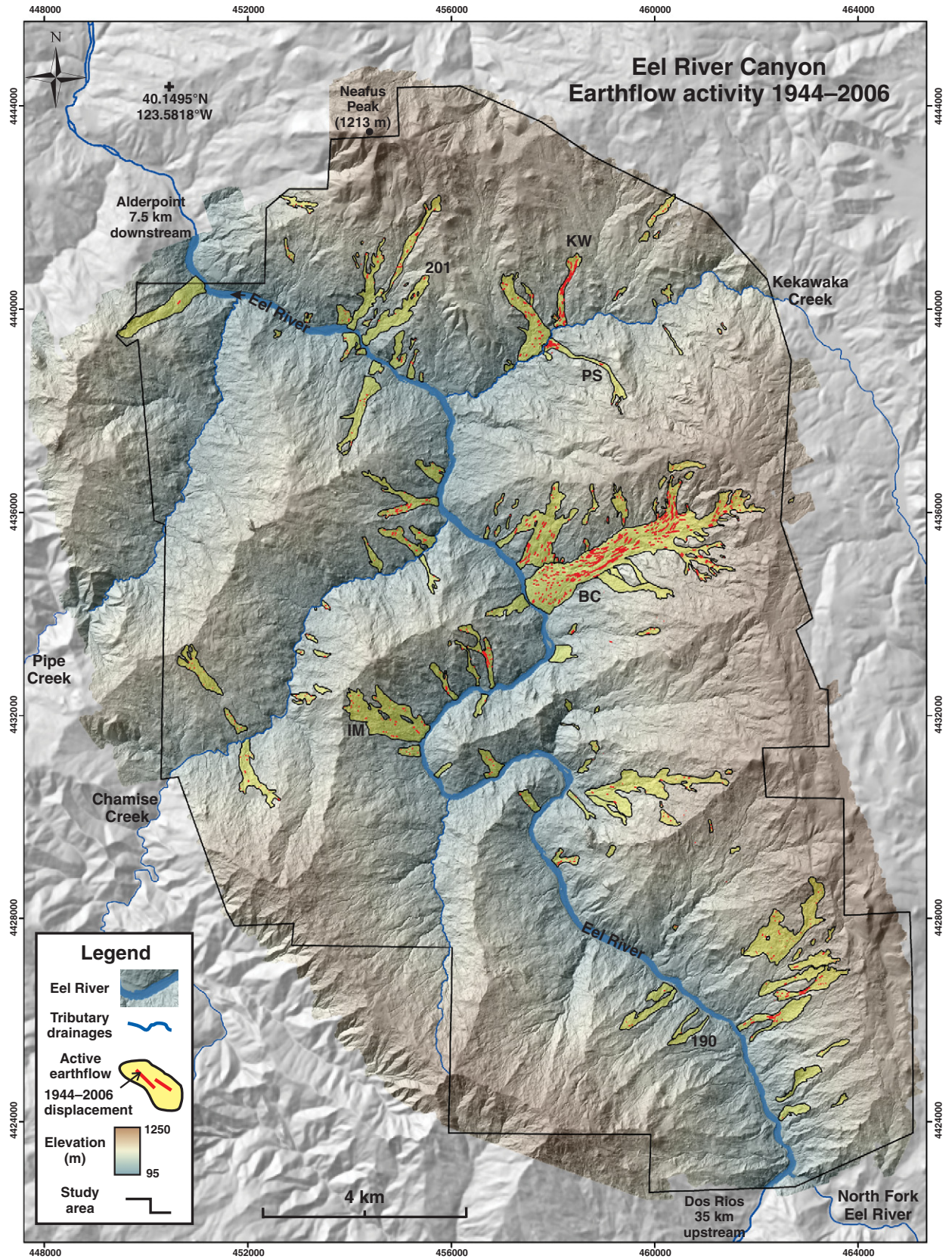


Figure 8. Map of the 226 km² study area, active earthflows, and tree displacements, from 1944 to 2006. Extent of light detection and ranging (LiDAR) coverage is shown as shaded relief, colored by elevation. Specific earthflows: Boulder Creek (BC), Island Mountain (IM), Mile 201, Kekawaka (KW), Penstock (PS), Mile 190.5 (190). Background image is 30 m grid shaded relief. Coordinates are UTM Zone 10N.

Figure 9. (A) Histogram of 998 tree displacements mapped across the field area. (B) Histogram of rectification errors, calculated from the offset between stable features on the photo and light detection and ranging (LiDAR) data. Interquartile range (IQR) is middle 50% of data. Note the scale change from parts A to B.

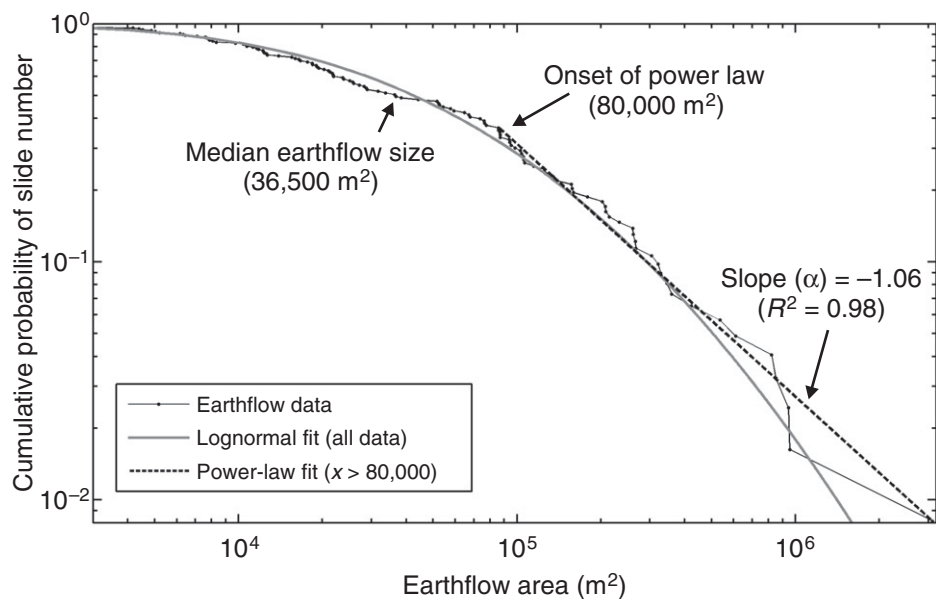
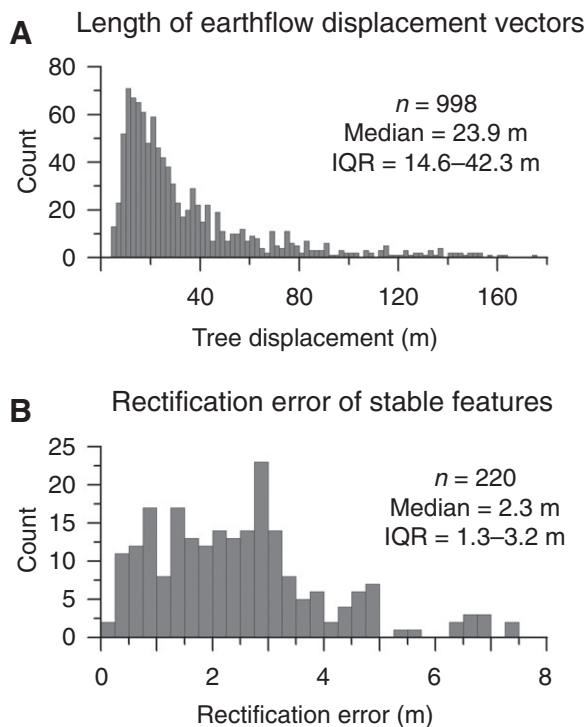


Figure 10. Distribution of earthflow areas. Cumulative probability plot of earthflow area, showing the lognormal fit over the whole data set, and a power-law fit to earthflow areas exceeding $80,000 m^2$.

Given the strong northwest-trending structural control on topography, we plotted the aspect of all 4 m pixels within the study area to determine whether this biased the aspect of earthflows. To properly compare the topographic trend with earthflow terrain, we identified the aspect of all 4 m pixels within active earthflows, but did not

discriminate by individual earthflow as in Figure 13A. Figure 13B highlights the asymmetry of regional aspect; the oblate circular rose diagram shows a bimodal distribution with slight preference for cells facing southwest. The mean direction of all topography is 246° , with a small mean resultant vector of 0.04, such that this ap-

parent preferred orientation of the terrain is not significant at $\alpha = 0.05$. The amalgamated earthflow terrain (Fig. 13B) has a pronounced bias to the southwest, with a mean direction vector of 218° , and resultant vector of 0.31, and is therefore significant at $\alpha = 0.05$.

Earthflow Sediment Flux

We estimated an average sediment flux of $120,000 \pm 10,000 m^3/yr$ (errors summed in quadrature) for 62 earthflows that discharge directly into a channel or creek (see Table DR1 [see footnote 1]) and thus can be considered tightly connected to the fluvial system. These earthflows have a combined area of $13.6 km^2$ (6.0% of the study area). This equates to a sediment yield for the 62 earthflow features of $19,000 \pm 2000, t km^{-2} yr^{-1}$, or a rock erosion rate of $\sim 7.6 mm/yr$ (bedrock density $2.5 g/cm^3$). When distributed over the study area of $226 km^2$, the mass translation of active earthflows generates an average regional sediment yield of $1100 t km^{-2} yr^{-1}$ ($\sim 0.45 mm/yr$). This rate is half of the $2200 t km^{-2} yr^{-1}$ suspended sediment yield calculated for the Eel River (1950–2000) by Wheatcroft and Sommerfield (2005). Hence, across our study area from 1944 to 2006, 6% of the terrain supplies approximately half of the sediment to channels.

DISCUSSION

Erosion and Sediment Delivery

Our results show that from 1944 to 2006, large, slow-moving earthflows were the primary process of erosion along the main stem Eel River, preferentially occurring in weak mélangé lithology. Mass translation by earthflows contributed $\sim 120,000 m^3/yr$ ($\sim 250,000 t/yr$) to the channel network in our study area. The sediment yield from the $13.6 km^2$ of active earthflows in Eel Canyon ($19,000 t km^{-2} yr^{-1}$) is similar to a comparable photogrammetric study (1941–1975) by Kelsey (1978) of Van Duzen earthflows ($24,900 t km^{-2} yr^{-1}$). When averaged over the $226 km^2$ study area, sediment delivery via active earthflows ($1100 t km^{-2} yr^{-1}$) accounts for approximately half the average sediment yield of the Eel River catchment during the second half of the twentieth century ($2200 t km^{-2} yr^{-1}$), despite earthflows encompassing just 6% of the study area terrain.

We attribute the additional suspended sediment yield ($\sim 50\%$) to both fluvial erosion of the earthflow surfaces, and erosion from the nonearthflow portion ($\sim 94\%$) of our study area in the form of gullies, streambank erosion, soil creep, and isolated shallow landslides. In hard

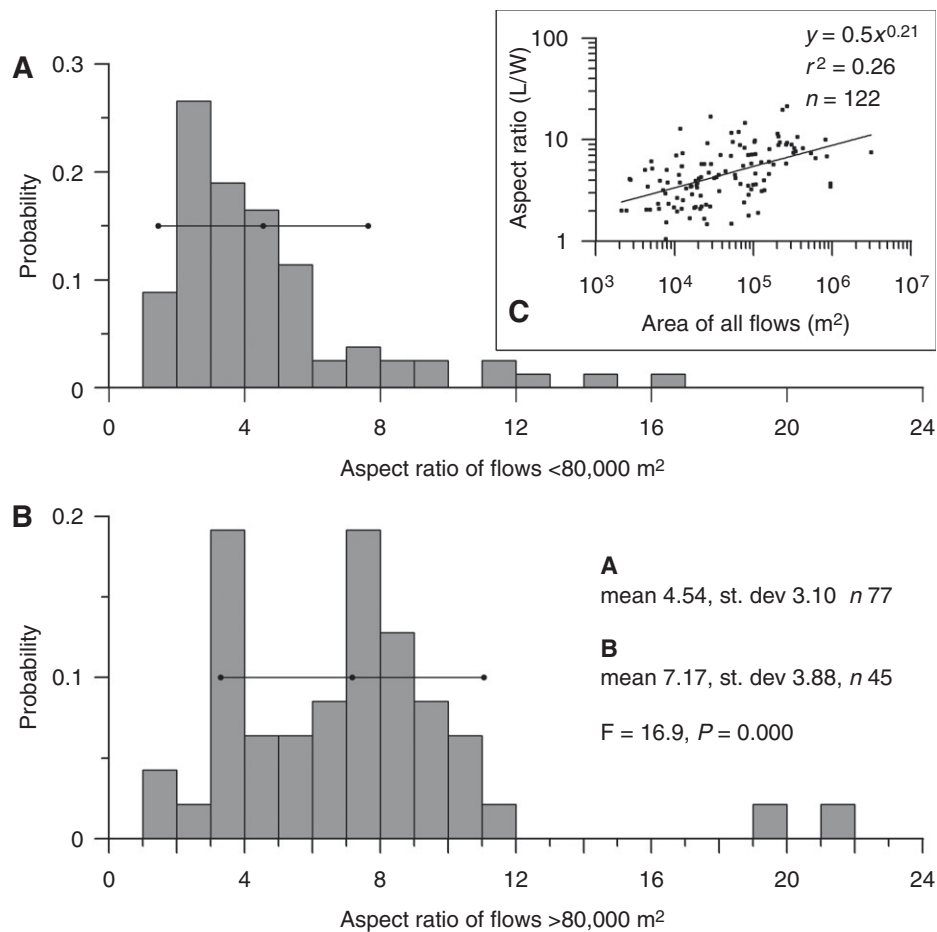


Figure 11. Earthflow shape aspect ratio. (A) Histogram of earthflow aspects with area <80,000 m². (B) Histogram of earthflow aspects with area >80,000 m². In A and B, horizontal bar shows mean ± 1 standard deviation. (C) Log-log plot showing dependence of earthflow aspect ratio on earthflow area.

topography, steep ridge and valley morphology suggests that debris flows are a primary erosional process, although such terrain was sparse in our field area (Fig. 3; Table 1). There is potential for fluvial erosion of the surface of active earthflows through localized gully (Kelsey, 1978; Schwab et al., 2008; Roering et al., 2009), although we did not account for this in our estimates of earthflow mass movement. In other studies of northern California earthflows, estimates of fluvial erosion of the earthflow surface ranged from 10% (Nolan and Janda, 1995) to 50% (Kelsey, 1978) of the total earthflow sediment flux. We predict our main stem Eel River study site would fall somewhere between these values—the earthflows along the Eel River are not as active or as incised as those along the Van Duzen River during the time of Kelsey's (1978) study, but they have higher rates of activity than those in Redwood Creek as documented by Nolan and Janda (1995). Therefore, the actual sediment yield from the 6% of active earth-

flow terrain could exceed 30,000 t km⁻² yr⁻¹ (~12 mm/yr) if fluvial erosion and gullying from the earthflow surface is taken into account.

We found that 6% of the landscape covered by active earthflows contributed at least 50% of the basinwide averaged suspended sediment yield. The ratio of fractional earthflow area to the fraction of earthflow-derived suspended sediment for the Eel River study site (6:50) approximates that found by Kelsey (1978) in the Van Duzen watershed (1:10). Both studies illustrate that the surface of active earthflows in Franciscan mélangé erode an order of magnitude more rapidly than catchment-averaged values, highlighting the highly erosive nature of earthflows. This rapid rate of erosion indicates that earthflows evolve at unsustainably fast rates over periods beyond several hundred years (Kelsey, 1978; Mackey et al., 2009) and so risk exhausting their supply of source material. The legacy of cycles of rapid erosion followed by lengthy periods of dormancy is reflected in the ubiquity

of inactive earthflow features in the landscape. Earthflow movement may be the dominant local erosional process for only a brief time.

Our 62 yr study period averages across decadal-scale variation in earthflow movement and does not capture potential fluctuations in earthflow activity over longer time scales. Bovis and Jones (1992) used tree ring data and tephrochronology to correlate earthflow movement with long-term (10²–10⁴ yr) changes in climate, and it is possible that earthflows in the Eel River were more active during the cooler and wetter climatic conditions during the Last Glacial Maximum (e.g., Adam and West, 1983; Barron et al., 2003). This does not require that inactive earthflow terrain be a relic of past climatic conditions, however, because other mechanisms, such as internal forcing within individual earthflows, can account for the distribution of earthflow activity we observe today (see section “Long-Term Earthflow Evolution” below).

An important finding is that 1.3% of the study area (17% of the total active earthflow area) moved during the study period but did not reach active channels. Earthflows that redistribute material on hillslopes but do not deliver sediment directly to channels are an important consideration when calculating sediment budgets. These unconnected earthflows may predispose the terrain to erosion by other processes, such as localized gully (Schwab et al., 2008), or ultimately lead to reactivation of larger earthflows by changing the distribution of stress on the hillslopes.

Brown and Ritter (1971) noted that the section of the Eel River watershed between Dos Rios and Scotia has greater sediment yield than the rest of the drainage due to the extensive mélangé lithology and the high number of active earthflows, meaning our study area along the main stem of the Eel River has a higher sediment yield than the Eel River catchment average. The proportion of regional erosion attributable to earthflow processes at the catchment scale may not be as large as our results suggest, but it cannot be quantified with available data.

Spatial Characteristics

Our results show that earthflows have a distinctive position in the landscape and characteristic spatial attributes, including planform shape and size distribution. The larger earthflows span ridge-to-channel length scales and are significantly more elongate than smaller flows. Earthflows that only partially span the length of the hillslope are more common higher on the hillslope toward the ridges, as opposed to the lower sections of hillslopes, where they are can interact with major gullies or creeks.

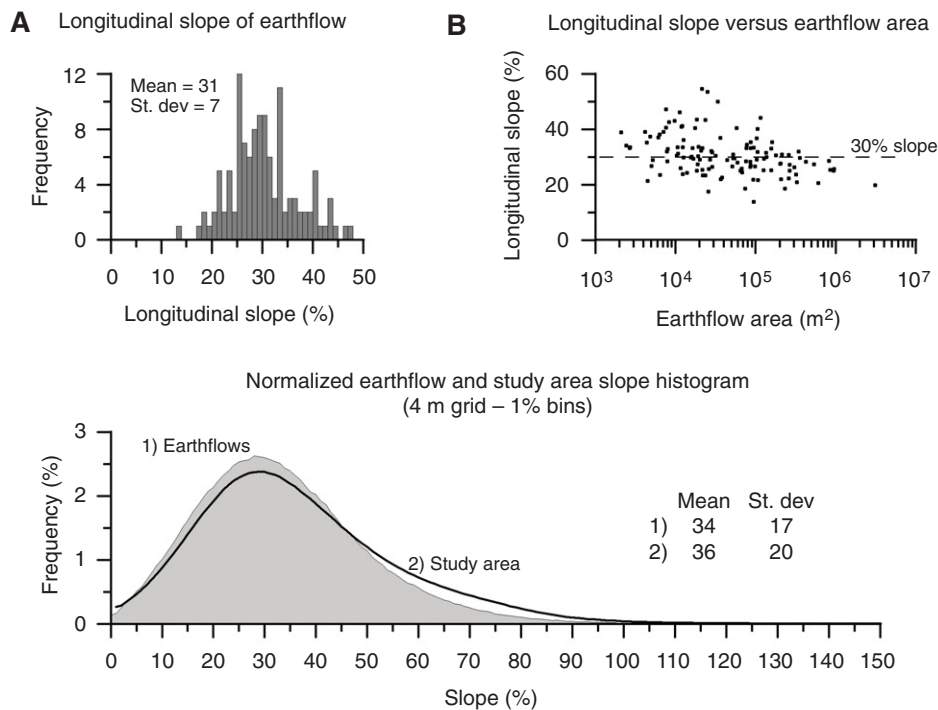


Figure 12. (A) Longitudinal slope of individual earthflows. (B) Comparison of earthflow longitudinal slope and area. (C) Histogram of slope of all 4 m pixels within the study area (black line), and all 4 m pixels within active earthflows (gray shading).

Although the sample size of our earthflow data set ($n = 122$) was modest in comparison to most landslide inventories (which can number in the thousands), our active earthflow map should be highly robust given the use of displaced features and LiDAR for defining slide margins. The probability distribution as a function of earthflow area is very well described by a lognormal distribution (Fig. 10). Lognormal distributions have been proposed for landslides in Redwood Creek, northern California (Kelsey et al., 1995), and for submarine failures on the U.S. Atlantic continental slope (Chaytor et al., 2009; ten Brink et al., 2009). Lognormal distributions have a characteristic size, and the median earthflow area for

our study site is 36,500 m², which equates to an earthflow with an approximate length and width of 400 m and 100 m, respectively, given a 4:1 length-to-width ratio.

Landslide size distributions have received considerable attention in the past decade because the magnitude and frequency of slope failure are primary controls on the rate of sediment flux from hillslopes (see review in Stark and Guzzetti, 2009) and can be used to quantify the risk of slope failure hazards. Landslide frequency generally decays as the inverse power of landslide area, both for a total landslide inventory and an event-specific distribution (e.g., Hovius et al., 1997; Stark and Hovius, 2001; Guzzetti

et al., 2002; Malamud et al., 2004a, 2004b; Korup, 2005a; Stark and Guzzetti, 2009). To our knowledge, the probability distribution of area has not been previously documented for large, slow-moving earthflows.

Frequently, a rollover or departure from power-law decay occurs for small landslide areas, which is attributed to either a change in process, or sampling artifact due to mapping resolution (Malamud et al., 2004a). The deviation from power-law behavior in our earthflow data set ($\sim 80,000$ m²) is well above the detection level of our methodology (< 1000 m²), suggesting a process-based explanation rather than mapping bias. The power-law exponent (α value) for large earthflows in our data set (1.06) is very low compared to other studies, which typically find α values of ~ 1.5 (Stark and Guzzetti, 2009). Our data set also shows that the onset of power-law behavior occurs at a much higher value of earthflow area ($\sim 80,000$ m²) than most landslide inventories, where the rollover occurs at 700–5000 m² (Hovius et al., 1997; Stark and Hovius, 2001; Malamud et al., 2004a; Stark and Guzzetti, 2009).

Once earthflows extend from the channel to the ridgeline, they can only increase their size by expanding laterally or incorporating tributary flows, which is not mechanically advantageous due to the planar nature of the hillslopes. Given the 2–3-km-long hillslopes in our study area and a length:width aspect ratio for larger flows of $\sim 7:1$, the expected maximum earthflow size range would be 0.6–1.2 km², consistent with our observations (Fig. 10). At the ~ 1 km² size, the cumulative earthflow size appears to diverge from the power-law trend (which is influenced by the Boulder Creek earthflow), suggesting that earthflows rarely attain such extents in this environment. We also note the Boulder Creek earthflow is an outlier on the lognormal fit. The large size of the Boulder Creek earthflow seems attributable to several large tributary lobes and fortuitous placement in a confined basin. We note that larger earthflows also have

TABLE 1. PROPORTION OF LITHOLOGY AND ACTIVE EARTHFLAWS (EF) ACROSS THE STUDY AREA

Lithology	Map unit	Area (m ²)	% study area	No. EF	EF area (m ²)	% EF area	% lithology active
Mélange—penetratively sheared meta-argillite	cm1	1.32×10^8	58.2	98	1.33×10^7	80.89	10.08
Broken formation (metasandstone)	cb1	5.75×10^7	25.4	16.5	2.10×10^6	12.71	3.65
Mélange (subequal argillite and sandstone)	cm2	1.88×10^7	8.3	2.5	5.64×10^5	3.42	3.00
Serpentinite	Sp	4.67×10^6	2.1	5	1.63×10^5	0.99	3.49
Greenstone	RB	4.14×10^6	1.8				
Block (unknown lithology)	RB	2.66×10^6	1.2				
Yolla Bolly (metasandstone)	ss	2.61×10^6	1.2				
Radiolarian chert	RB	1.02×10^6	0.5				
White rock (metasandstone)	ss	1.23×10^6	0.5				
Basaltic rocks	RB	6.86×10^5	0.3				
Broken formation (intact metasandstone)	cb1	4.16×10^5	0.2				
Chert	RB	5.57×10^5	0.2				
Blueschist blocks	RB	1.29×10^5	0.1				
		2.26×10^8	100.0	122	16.5×10^7		

Note: Map unit indicates representation in Figure 3. For detailed lithology descriptions, see McLaughlin et al. (2000).

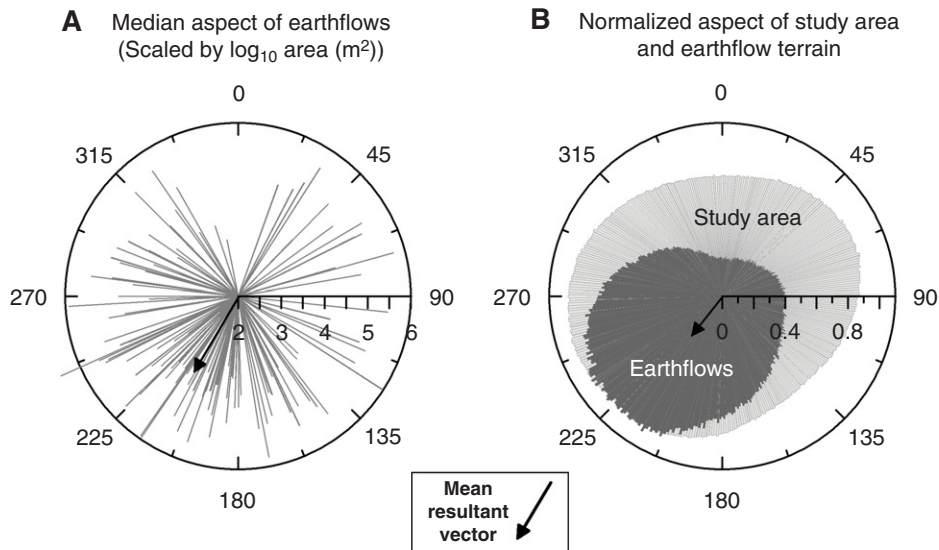


Figure 13. Aspect of earthflows and the study area. (A) Median aspect of 4 m pixels within each earthflow polygon, scaled by \log_{10} area (m²). Mean resultant vector is 210°. (B) Rose diagram of aspect of 4 m pixels across the study area, and all 4 m pixels within active earthflows (1° bins). Mean resultant vector of the earthflow terrain is 218°. Study area terrain does not have a significant mean direction.

lower longitudinal slopes than average (Fig. 11C), which may reflect greater interaction with channel/gully incision processes due to the increased drainage areas inherent to larger earthflows. Alternatively, the larger flows may be thicker, and require less slope to attain the same driving stress, or the longer transport zones of large earthflows may have less influence from toe buttressing, promoting earthflow sliding at lower gradients (Bovis and Jones, 1992).

Earthflows predominantly occur in fine-grained, clay-rich lithologies (Keefer and Johnson, 1983; Hungr et al., 2001), especially in argillaceous or altered volcanoclastic sediments (Glastonbury and Fell, 2008). Given the lithological variability across the study area, it is unsurprising that active earthflows preferentially occur in the sheared argillaceous mélangé (unit cm1 in Fig. 3), and 10% of this lithology is subject to active slope instability (Table 1). However, given the lack of bedrock exposure in this region, much of the lithological mapping was undertaken with aerial photograph interpretation, and slope morphology is a key metric in distinguishing between different mélangé units. McLaughlin et al. (2000) noted that the Central belt mélangé unit exhibits characteristic earthflow morphology, and used the rounded, poorly incised, lumpy, and irregular topography as a diagnostic feature during bedrock mapping. This introduces circularity when comparing earthflow activity across argillaceous mélangé units. More robust is the observed dichotomy between

processes of erosion in the argillaceous terrain compared to resistant sandstone outcrops, with earthflows absent in the latter (Table 1). Earthflows move around and between the harder mélangé blocks, leaving them as steep localized topographic highs extending out of the mélangé. The exposed sandstone blocks either weather away in place by rockfall processes, or they can fail catastrophically if they are sufficiently undermined by the surrounding earthflow-prone terrain. Larger, resistant sandstone outcrops at the kilometer-scale have well-incised drainages, and steeper slopes, emphasizing the contrasting erosional regimes that operate within different lithologies in the same landscape.

The mean longitudinal slope of the earthflows (31%) compares well with the data of Iverson and Major (1987), who reported a residual friction angle for sheared earthflow soil of ~33%. The mean longitudinal slope of the earthflows is less than the mean slope of all earthflow terrain (34%; Fig. 12C), probably due to roughness and hummocky topography on the earthflow surface. Compared to active earthflow terrain, the study area has a significant fraction of terrain steeper than 50%, as reflected by a heavier tail in the distribution of slopes (Fig. 12C). This is attributable to gorges, cliffs, and steeper sandstone units throughout the study area, i.e., locations not conducive to earthflow activity. The mean slope of all earthflow terrain in Figure 12C (34%) is very similar to the study area terrain (36%). The similarity of mean slopes for

earthflows and the study area supports our observation that much of the landscape has been modulated by earthflow processes, even if they are not currently active. A slope of 34%–36% may be an approximate limiting threshold slope for earthflow activity, and possibly represents the residual shear strength of the mélangé at the landscape scale (e.g., Skempton, 1964; Hutchinson, 1967; Carson and Petley, 1970). The relative scarcity of terraces in our study site (Fig. 8) supports the contention that many of the hillslopes adjust to threshold values as the Eel River incises (Korup et al., 2010). The fact that the very largest earthflows typically have lower longitudinal slopes (Fig. 12B) suggests that they are not simply relaxing back to a residual slope and potentially have increased erosional efficiency, as discussed previously herein.

The earthflows in our study site occur preferentially on south-southwest-facing slopes. Kelsey (1978) suggested that slopes with a southerly aspect are drier and do not support conifer growth, which preferentially stabilizes the north-facing slopes. Across our study area, lithology appears to have a stronger influence on vegetation than slope aspect, and many north-facing slopes have open grassland susceptible to earthflow activity (e.g., Fig. 5). The primary difference between northerly and southerly aspect is variation in incident solar radiation, so the preferred southerly aspect is plausibly attributable to differences in evaporation and soil moisture. This seems counterintuitive, given the dependence of earthflow movement on elevated pore pressures (e.g., Iverson and Major, 1987), which would presumably be greater on north-facing slopes. McSaveney and Griffiths (1987) suggested that drought may be a precursor to earthflow activity. They argued that deep desiccation cracks penetrate the earthflow mass during drought, providing easy conduits for water to travel deep into the earthflow mass when rainfall resumes. Following rainfall, surface moisture levels increase, desiccation cracks close, and the permeability of the earthflow surface decreases markedly. In the Eel River catchment, our field observations indicate that south-facing slopes become highly desiccated over the summer months, and surface cracks up to 50 mm wide extend to depths over 1 m. Northerly facing slopes do not dry to the same extent. This aspect-governed asymmetry of drying and soil moisture over the summer months may explain some of the southwestward aspect preference we observe in the active earthflows. Aspect-dependent seasonally increased permeability may also enhance weathering, leading to increased availability of readily mobilized regolith on south-facing slopes. The northerly facing slopes do have the morphology of dormant

earthflows, and have been active in the past, potentially under different climatic conditions.

Dip-slopes with weak bedding or structural defects can strongly control the directionality of slope stability (e.g., Pettinga, 1987). Structure throughout our study site consists of steeply dipping, highly-sheared, and tightly folded rocks striking to the northwest (McLaughlin et al., 2000). Structures such as bedding planes or foliation do not appear to control earthflow location, and the regional-scale structural grain does not have a significant effect (Fig. 13B).

Long-Term Earthflow Evolution

We combined the spatial distribution of earthflows, field observations, and analysis of LiDAR-derived topography to develop a conceptual model for the long-term evolution of earthflow-prone terrain. Due to the pervasive history of slope instability throughout our study site, we rarely observe earthflows that extend partially up a slope that are not within a larger, established (if dormant) earthflow complex (Figs. DR1–DR2 [see footnote 1]). Large active earthflows mostly extend from the channel to the ridge or a topographic break in slope (Iverson, 1986b). It is rare to observe a youthful earthflow actively retrogressing into a previously unfailed hillslope. The few examples of such earthflow behavior in our field site were generally retrogressing up broad ridgelines, establishing new earthflow basins (e.g., Mile 201 slide, Fig. 8). Once established, the architecture of an individual earthflow basin can persist in the landscape for significant periods of time, as evidenced by the many dormant earthflow features preserved (e.g., Fig. 4; Figs. DR1–DR2 [see footnote 1]).

Where active earthflows do not span channel to ridge, our data show that they are preferentially confined to the upper sections of hillslopes (Fig. 8; Table DR1 [see footnote 1]) and appear to constitute partial reactivation of older, largely dormant earthflow features. There are numerous examples of earthflows initiating high on the hillslope. For example, Kelsey (1978) described smaller earthflows confined to midslopes, and Putnam and Sharp (1940) described earthflows in Ventura County, California, starting on the upper slopes and moving downhill. In our study site, the New 190.5 slide (shown in Fig. 4) reportedly started moving in 1952. Slide debris progressively moved downslope and eventually reached the railway near the river in 1966 (Scott, 1973).

We argue that the observations of smaller flows preferentially occurring on upper slopes, and the past descriptions of earthflow activity support a top-down driver of long-term earthflow evolution. Given that rates of sediment

yields from earthflows are significantly faster than regional erosion rates, an active earthflow will eventually exhaust its source material and become dormant. We suggest that reactivation of an earthflow complex is driven from the upper slopes, and earthflow activity propagates downslope, possibly via undrained loading (Hutchinson and Bhandari, 1971), rather than through toe perturbation (e.g., channel incision) propagating upslope. The amount of readily mobilized source sediment that can be incorporated into an earthflow, as governed by weathering rates and the conversion of bedrock to regolith, may be the ultimate control on the location and rate at which earthflows evolve, or the periodicity with which they are active.

Active earthflows frequently exhibit pervasive surficial gully networks (Figs. 4, 5, and 8; Figs. DR1–DR2 [see footnote 1]) and commonly have large axial gullies that run down the margin or center of earthflows. Although the role of gully networks in removing sediment from active earthflows can be significant (Kelsey, 1978; Roering et al., 2009), the relations and feedbacks between gullying and earthflow mobility have not been well quantified. For example, do gullies cause minor instabilities that coalesce to form major flows? Alternatively, can gullies, by eroding the earthflow mass, lower the driving stresses on the flow and contribute to stability?

It is clear that gullies and creeks play a major role by continuing to perturb and incise into earthflow material once movement has ceased (Figs. 4; Figs. DR1–DR2 [see footnote 1]), and we observed surficial gully networks propagating through the transport zones and source zones of dormant flows (Figs. DR1–DR2 [see footnote 1]). We argue that propagation of the gully network into the amphitheater-like, earthflow material-starved source zones of dormant earthflows promotes dissection of residual material, enhances bedrock weathering, and eventually increases the availability of easily mobilized soil and regolith feeding into the source zone. These discontinuous gullies are not connected to the channel network and act to disturb and redistribute material on the upper earthflow slopes, rather than act as a conduit for significant sediment removal. Redistributed material can then coalesce in the source zone via small slumps and flows from the headscarp and exposure of bedrock underlying the source zone, increase local topographic loading, commence downslope movement, and ultimately reactivate the whole earthflow. In Figure 14, we present a conceptual model of the long-term cyclical evolution of an earthflow, governed by the availability of source material, and the ability of gully networks to propagate through dormant

earthflows. Figures DR1 and DR2 (see footnote 1) show examples from the field site reflecting each stage of the process.

We start in Figure 14A with an active earthflow, such as the larger flows mapped in Figure 8. After prolonged movement, the readily mobilized source material becomes exhausted (Fig. 14B), and the earthflow mass thins and reduces driving stresses, which leads to stability. Once the earthflow mass is stable, axial gullies propagate up through the easily erodible earthflow body, while weathering proceeds in the newly exposed rock in the source zone and headscarp walls. This process continues (Fig. 14C), and a network of smaller gullies propagates up into the earthflow source zone, destabilizing the recently weathered rock and regolith and generating several small earthflows. These small earthflows coalesce in the source zone, and move downslope, reactivating the earthflow complex. In essence, the slopes are delicately balanced, and some destabilization, redistribution of mass, and loading at the top of the earthflow can reactivate the whole feature.

We envisage a period of earthflow activity of decades to centuries, followed by dormancy of thousands of years. During this time, the channel at the toe of the earthflow incises at rates proportional to regional channel incision, and this ensures maintenance of the critical slope required for multiple cycles of earthflow activity. The rate of channel incision likely controls the downward propagation of the earthflow failure plane or shear zone. Channel incision at the toes of earthflow-prone hillslopes is necessary to generate the relief required for persistent earthflow activity, and yet episodes of rapid earthflow activity and dormancy appear to be modulated by the availability of readily mobilized regolith on the upper hillslopes.

CONCLUSION

Earthflows dominate the erosion, morphology, and evolution of the landscape along the main stem Eel River. Using airborne LiDAR and aerial photos, we objectively documented regional earthflow activity and sediment flux across 226 km² of earthflow-prone terrain. We find that 7.3% of the study area was active in the period 1944–2006, and 6% of the study area is composed of earthflows discharging into the channel network. Movement, as documented from displaced shrubs, had a median velocity of 0.4 m/yr over the 62 yr interval, although the distribution of displacement vectors was heavily positively skewed and ranged up to 2.8 m/yr.

Earthflows in our study site have characteristic spatial attributes, which include a

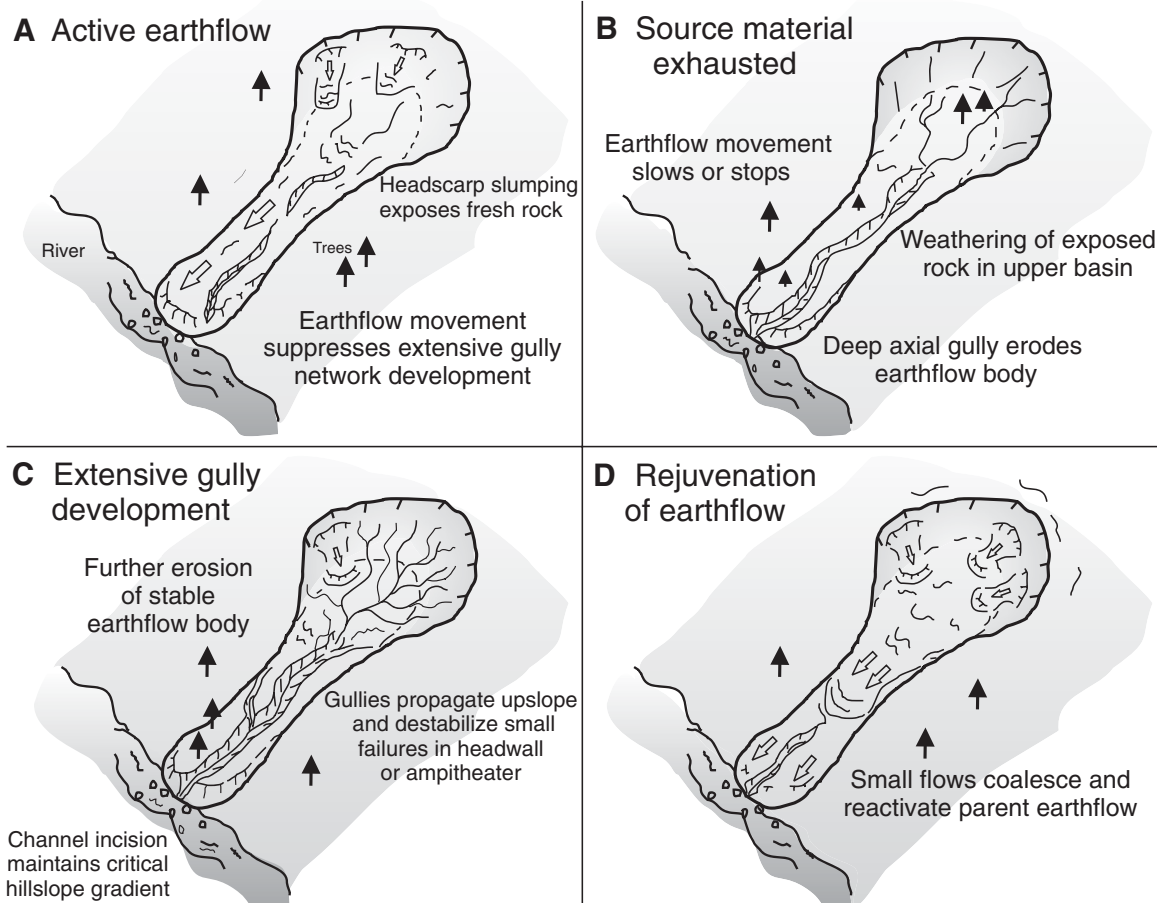


Figure 14. Conceptual earthflow evolution model. (A) Active earthflow is being supplied with material from small slumps and failures in the upper amphitheater. (B) Eventually, the source material is exhausted, and gullies begin to erode the earthflow body. (C) Gullies propagate into the source area, destabilizing and mobilizing the weathered slopes. (D) Small flows coalesce in the upper amphitheater source area and reactivate the earthflow transport zone.

lognormal size distribution, preferential south-southwesterly aspect, and strong association with sheared argillaceous lithology. The earthflows have a slope distribution that is similar to the slope distribution of the study area, although the mean slope of earthflow terrain (34%) is slightly less than the study area (36%), suggesting that many of the slopes approach a critical or threshold value. Larger earthflows (>250,000 m²) typically span from channel to ridge, whereas the majority of earthflows that do not are located higher on the hillslopes and are not connected to channels. The large earthflows tend to be less steep and are significantly more elongate than smaller features.

Averaged across the 226 km² studied section of the Eel River, mass movement by earthflows generated a sediment yield of 1100 t km⁻² yr⁻¹. This is half of the estimated regional sediment yield (2200 t km⁻² yr⁻¹), despite active earthflows accounting for only 6% of the study area.

The sediment yield from earthflow areas alone was 19,000 t km⁻² yr⁻¹ (rock erosion rate 7.6 mm/yr), and could potentially double by accounting for fluvial erosion from the earthflow surface. Given that the sediment yield from active earthflows can exceed the regional sediment yield by an order of magnitude, we envisage earthflow activity as being intermittent, separated by long periods of dormancy. Most of the argillaceous terrain in our study site shows topographic evidence of earthflows, suggesting that locations of activity can migrate through the landscape. In contrast to many other styles of slope failures, earthflows appear to reactivate from the top when there is sufficient readily mobilized material; a top-down perturbation can reactivate the whole earthflow. We suggest that long-term availability of readily mobilized source sediment is the primary control on cycles of earthflow activity and evolution.

ACKNOWLEDGMENTS

This research was funded by a National Science Foundation (NSF) grant (Geomorphology and Land Use Dynamics, EAR-0447190) to J. Roering. B. Mackey was partially supported by the "Fulbright EQC Award in Natural Disaster Research" from New Zealand. The LiDAR data were acquired by the National Center for Airborne Laser Mapping (NCALM) in 2006. We thank Calvin and Wendy Stewart for field access and generous hospitality, and the Lone Pine and Island Mountain ranches for field access. We benefited from fruitful discussions with Harvey Kelsey and Jim McKean over the course of this research. We thank Harvey Kelsey, Bill Haneberg, Grant Meyer, and Associate Editor Jon Major for insightful reviews that greatly improved this manuscript.

REFERENCES CITED

- Adam, D.P., and West, G.J., 1983, Temperature and precipitation estimates through the last glacial cycle from Clear Lake, California, pollen data: *Science*, v. 219, no. 4581, p. 168–170, doi: 10.1126/science.219.4581.168.
- Angeli, M.G., Gasparetto, P., Menotti, R.M., Pasuto, A., and Silvano, S., 1996, A visco-plastic model for slope

- analysis applied to a mudslide in Cortina d'Ampezzo, Italy: *Quarterly Journal of Engineering Geology*, v. 29, p. 233–240, doi: 10.1144/GSL.QJEGH.1996.029.P3.06.
- Barron, J.A., Heusser, L., Herbert, T., and Lyle, M., 2003, High-resolution climatic evolution of coastal northern California during the past 16,000 years: *Paleoceanography*, v. 18, no. 18, 1020, 19 p., doi: 10.1029/2002PA000768.
- Baum, R.L., Fleming, R.W., and Johnson, A.M., 1993, Kinematics of the Aspen Grove landslide, Ephraim Canyon, central Utah, *in* *Landslide Processes in Utah—Observation and Theory*: U.S. Geological Survey Bulletin 1842, p. F1–F34.
- Benda, L., and Dunne, T., 1997, Stochastic forcing of sediment supply to channel networks from landsliding and debris flow: *Water Resources Research*, v. 33, no. 12, p. 2849–2863, doi: 10.1029/97WR02388.
- Booth, A.M., Roering, J.J., and Perron, J.T., 2009, Automated landslide mapping using spectral analysis and high-resolution topographic data: Puget Sound lowlands, Washington, and Portland Hills, Oregon: *Geomorphology*, v. 109, no. 3–4, p. 132–147, doi: 10.1016/j.geomorph.2009.02.027.
- Bovis, M.J., and Jones, P., 1992, Holocene history of earthflow mass movements in south-central British Columbia—The influence of hydroclimatic changes: *Canadian Journal of Earth Sciences*, v. 29, no. 8, p. 1746–1755.
- Brown, W.M., and Ritter, J.R., 1971, *Sediment Transport and Turbidity in the Eel River Basin*. California: U.S. Geological Survey Water-Supply Paper 1986, 67 p.
- Brückl, E., and Sehidegger, A.E., 1973, Application of theory of plasticity to slow mud flows: *Geotechnique*, v. 23, no. 1, p. 101–107, doi: 10.1680/geot.1973.23.1.101.
- California Department of Water Resources, 1970, *Middle Fork Eel River Landslides Investigation*: California Department of Water Resources, Northern District, Memorandum Report, 117 p.
- Carranco, L., and Beard, E., 1981, *Genocide and Vendetta—The Round Valley Wars of Northern California*: Norman, Oklahoma, University of Oklahoma Press, 403 p.
- Carson, M.A., and Petley, D.T., 1970, The existence of threshold slopes in the denudation of the landscape: *Transactions of the Institute of British Geographers*, v. 49, p. 77–95.
- Carter, W.E., Shrestha, R.L., and Slatton, K.C., 2007, Geotectic laser scanning: *Physics Today*, v. 60, no. 12, p. 41–47, doi: 10.1063/1.2825070.
- Chandler, J.H., and Brunsden, D., 1995, Steady-state behavior of the Black-Ven mudslide—The application of archival analytical photogrammetry to studies of landform change: *Earth Surface Processes and Landforms*, v. 20, no. 3, p. 255–275, doi: 10.1002/esp.3290200307.
- Chaytor, J.D., ten Brink, U.S., Solow, A.R., and Andrews, B.D., 2009, Size distribution of submarine landslides along the US Atlantic margin: *Marine Geology*, v. 264, no. 1–2, p. 16–27, doi: 10.1016/j.margeo.2008.08.007.
- Coe, J.A., Ellis, W.L., Godt, J.W., Savage, W.Z., Savage, J.E., Michael, J.A., Kibler, J.D., Powers, P.S., Lidke, D.J., and Debray, S., 2003, Seasonal movement of the Slumgullion landslide determined from global positioning system surveys and field instrumentation, July 1998–March 2002: *Engineering Geology*, v. 68, no. 1–2, p. 67–101, doi: 10.1016/S0013-7952(02)00199-0.
- Craig, D., 1981, Mudslide plug flow within channels: *Engineering Geology*, v. 17, no. 4, p. 273–281, doi: 10.1016/0013-7952(81)90003-X.
- Cruden, D.M., and Varnes, D.J., 1996, Landslide types and processes, *in* Turner, A.K., and Schuster, R.L., eds., *Landslides: Investigation and Mitigation*: Washington, D.C., National Academy Press, p. 36–71.
- Dietrich, W.E., and Dunne, T., 1978, Sediment budget for a small catchment in mountainous terrain: *Zeitschrift für Geomorphologie*, v. 29, p. 191–206.
- Dietrich, W.E., Bellugi, D.G., Sklar, L.S., Stock, J.D., Heimath, A.M., and Roering, J.J., 2003, Geomorphic transport laws for predicting landscape form and dynamics, *in* Wilcock, P., and Iverson, R.M., eds., *Prediction in Geomorphology*: Washington D.C., American Geophysical Union, p. 103–132.
- Dumitru, T.A., 1991, Major Quaternary uplift along the northernmost San Andreas fault, King Range, northwestern California: *Geology*, v. 19, no. 5, p. 526–529, doi: 10.1130/0091-7613(1991)019<0526:MQUATN>2.3.CO;2.
- Dwyer, M.J., Scott, R.G., and Lorens, P.J., 1971, *Landslide Conditions and Related Sediment Production on the Eel River: Red Bluff, California*, California Department of Water Resources, Northern District, 69 p.
- Fuller, T.K., Perg, L.A., Willenbring, J.K., and Lepper, K., 2009, Field evidence for climate-driven changes in sediment supply leading to strath terrace formation: *Geology*, v. 37, no. 5, p. 467–470, doi: 10.1130/G25487A.1.
- Furlong, K.P., and Govers, R., 1999, Ephemeral crustal thickening at a triple junction: The Mendocino crustal conveyor: *Geology*, v. 27, no. 2, p. 127–130, doi: 10.1130/0091-7613(1999)027<0127:ECTAAT>2.3.CO;2.
- Furlong, K.P., and Schwartz, S.Y., 2004, Influence of the Mendocino triple junction on the tectonics of coastal California: *Annual Review of Earth and Planetary Sciences*, v. 32, p. 403–433, doi: 10.1146/annurev.earth.32.101802.120252.
- Glastonbury, J., and Fell, R., 2008, Geotechnical characteristics of large slow, very slow, and extremely slow landslides: *Canadian Geotechnical Journal*, v. 45, no. 7, p. 984–1005, doi: 10.1139/T08-021.
- González-Diez, A., Remondo, J., de Teran, J.R.D., and Cendrero, A., 1999, A methodological approach for the analysis of the temporal occurrence and triggering factors of landslides: *Geomorphology*, v. 30, no. 1–2, p. 95–113, doi: 10.1016/S0169-555X(99)00047-1.
- Guzzetti, F., Malamud, B.D., Turcotte, D.L., and Reichenbach, P., 2002, Power-law correlations of landslide areas in central Italy: *Earth and Planetary Science Letters*, v. 195, no. 3–4, p. 169–183, doi: 10.1016/S0012-821X(01)00589-1.
- Haneberg, W.C., Cole, W.F., and Kasali, G., 2009, High-resolution lidar-based landslide hazard mapping and modeling, UCSF Parnassus Campus, San Francisco, USA: *Bulletin of Engineering Geology and the Environment*, v. 68, no. 2, p. 263–276, doi: 10.1007/s10064-009-0204-3.
- Hilley, G.E., Burgmann, R., Ferretti, A., Novati, F., and Rocca, F., 2004, Dynamics of slow-moving landslides from permanent scatterer analysis: *Science*, v. 304, no. 5679, p. 1952–1955, doi: 10.1126/science.1098821.
- Hovius, N., Stark, C.P., and Allen, P.A., 1997, Sediment flux from a mountain belt derived by landslide mapping: *Geology*, v. 25, no. 3, p. 231–234, doi: 10.1130/0091-7613(1997)025<0231:SFFAMB>2.3.CO;2.
- Hovius, N., Stark, C.P., Tutton, M.A., and Abbott, L.D., 1998, Landslide-driven drainage network evolution in a pre-steady-state mountain belt: Finisterre Mountains, Papua New Guinea: *Geology*, v. 26, no. 12, p. 1071–1074, doi: 10.1130/0091-7613(1998)026<1071:LDDNEI>2.3.CO;2.
- Hungr, O., Evans, S.G., Bovis, M.J., and Hutchinson, J.N., 2001, A review of the classification of landslides of the flow type: *Environmental & Engineering Geoscience*, v. 7, no. 3, p. 221–238.
- Hutchinson, J.N., 1967, The free degradation of London clay cliffs, *in* *Proceedings of the Geotechnical Conference*: Oslo, Norwegian Geotechnical Institute, p. 113–118.
- Hutchinson, J.N., and Bhandari, R.K., 1971, Undrained loading, a fundamental mechanism of mudflows and other mass movements: *Geotechnique*, v. 21, no. 4, p. 353–358, doi: 10.1680/geot.1971.21.4.353.
- Iverson, R.M., 1986a, Dynamics of slow landslides: A theory for time-dependent behavior, *in* Abrahams, A.D., ed., *Hillslope Processes*: Boston, Massachusetts, Allen and Unwin, p. 297–317.
- Iverson, R.M., 1986b, Unsteady, nonuniform landslide motion: 1. Theoretical dynamics and the steady datum state: *The Journal of Geology*, v. 94, no. 1, p. 1–15, doi: 10.1086/629006.
- Iverson, R.M., 1986c, Unsteady, nonuniform landslide motion: 2. Linearized theory and the kinematics of transient-response: *The Journal of Geology*, v. 94, no. 3, p. 349–364, doi: 10.1086/629034.
- Iverson, R.M., 2005, Regulation of landslide motion by dilatancy and pore pressure feedback: *Journal of Geophysical Research—Earth Surface*, v. 110, no. F2, F02015, 16 p., doi: 10.1029/2004JF000268.
- Iverson, R.M., and Major, J.J., 1987, Rainfall, groundwater-flow, and seasonal movement at Minor Creek landslide, northwestern California—Physical interpretation of empirical relations: *Geological Society of America Bulletin*, v. 99, no. 4, p. 579–594, doi: 10.1130/0016-7606(1987)99<579:RGFASM>2.0.CO;2.
- Jayko, A.S., Blake, M.C., McLaughlin, R.J., Ohlin, H.N., Ellen, S.D., and Kelsey, H.M., 1989, *Reconnaissance Geologic Map of the Covelo 30-by 60-Minute Quadrangle, Northern California*: U.S. Geological Survey Miscellaneous Field Investigation Map MF-2001, scale 1:100,000.
- Keefer, D.K., 1984, Landslides caused by earthquakes: *Geological Society of America Bulletin*, v. 95, no. 4, p. 406–421, doi: 10.1130/0016-7606(1984)95<406:LCBE>2.0.CO;2.
- Keefer, D.K., and Johnson, A.M., 1983, *Earth Flows: Morphology, Mobilization and Movement*: U.S. Geological Survey Professional Paper 1256, 56 p.
- Kelsey, H.M., 1977, *Landsliding, Channel Changes, Sediment Yield and Land Use in the Van Duzen River Basin, North Coastal California, 1941–1975* [Ph.D. thesis]: Santa Cruz, University of California, 370 p.
- Kelsey, H.M., 1978, Earthflows in Franciscan mélange, Van Duzen River basin, California: *Geology*, v. 6, no. 6, p. 361–364.
- Kelsey, H.M., 1980, A sediment budget and an analysis of geomorphic process in the Van Duzen River Basin, north coastal California, 1941–1975—Summary: *Geological Society of America Bulletin*, v. 91, no. 4, p. 190–195.
- Kelsey, H.M., and Carver, G.A., 1988, Late Neogene and Quaternary tectonics associated with northward growth of the San Andreas transform-fault, northern California: *Journal of Geophysical Research—Solid Earth and Planets*, v. 93, no. B5, p. 4797–4819, doi: 10.1029/JB093iB05p04797.
- Kelsey, H.M., Coghlan, M., Pitlick, J., and Best, B., 1995, Geomorphic analysis of streamside landslides in the Redwood Creek Basin, northwestern California, *in* Nolan, K.M., Kelsey, H.M., and Marron, D.C., eds., *Geomorphic Processes and Aquatic Habitat in the Redwood Creek Basin, Northwestern California*: U.S. Geological Survey Professional Paper 1454-J, p. J1–J12.
- Korup, O., 2005a, Distribution of landslides in southwest New Zealand: *Landslides*, v. 2, no. 1, p. 43–51, doi: 10.1007/s10346-004-0042-0.
- Korup, O., 2005b, Large landslides and their effect on sediment flux in South Westland, New Zealand: *Earth Surface Processes and Landforms*, v. 30, no. 3, p. 305–323.
- Korup, O., 2006, Rock-slope failure and the river long profile: *Geology*, v. 34, no. 1, p. 45–48.
- Korup, O., Densmore, A.L., and Schlunegger, F., 2010, The role of landslides in mountain range evolution: *Geomorphology*, v. 120, no. 1–2, p. 77–90, doi: 10.1016/j.geomorph.2009.09.017.
- Larsen, L.J., Montgomery, D.R., and Korup, O., 2010, Landslide erosion controlled by hillslope material: *Nature Geoscience*, v. 3, no. 4, p. 247–251, doi: 10.1038/ngeo776.
- Lave, J., and Burbank, D., 2004, Denudation processes and rates in the Transverse Ranges, southern California: Erosional response of a transitional landscape to external and anthropogenic forcing: *Journal of Geophysical Research—Earth Surface*, v. 109, F01006, 31 p.
- Lawson, A.C., 1908, *The California Earthquake of April 18, 1906*: Report of the State Earthquake Investigation Commission Publication 87: Washington, D.C., Carnegie Institution of Washington, 1, 451 p.
- Lehre, A.K., and Carver, G.A., 1985, Thrust faulting and earthflows: Speculations on the sediment budget of a tectonically active drainage basin, *in* Savina, M.E., ed., *Redwood Country: American Geomorphological Conference, Field Trip Guidebook 1985*: Arcata, California, p. 169–183.
- Lisle, T.E., 1990, The Eel River, northwestern California; high sediment yields from a dynamic landscape, *in* Wolman, M.G., and Riggs, H.C., eds., *Surface Water Hydrology*, p. 0–1, *The Geology of North America: Boulder, Colorado*, Geological Society of America, p. 311–314.

Earthflow activity and erosion, Eel River, California

- Lock, J., Kelsey, H., Furlong, K., and Woolace, A., 2006, Late Neogene and Quaternary landscape evolution of the northern California Coast Ranges: Evidence for Mendocino triple junction tectonics: *Geological Society of America Bulletin*, v. 118, no. 9–10, p. 1232–1246, doi: 10.1130/B25885.1.
- Mackey, B.H., Roering, J.J., and McKean, J.A., 2009, Long-term kinematics and sediment flux of an active earthflow, Eel River, California: *Geology*, v. 37, no. 9, p. 803–806, doi: 10.1130/G30136A.1.
- Malamud, B.D., Turcotte, D.L., Guzzetti, F., and Reichenbach, P., 2004a, Landslide inventories and their statistical properties: *Earth Surface Processes and Landforms*, v. 29, no. 6, p. 687–711, doi: 10.1002/esp.1064.
- Malamud, B. D., Turcotte, D. L., Guzzetti, F., and Reichenbach, P., 2004b, Landslides, earthquakes, and erosion: *Earth and Planetary Science Letters*, v. 229, no. 1–2, p. 45–59.
- Malet, J.P., Maquaire, O., and Calais, E., 2002, The use of global positioning system techniques for the continuous monitoring of landslides: Application to the Super-Sauze earthflow (Alpes-de-Haute-Provence, France): *Geomorphology*, v. 43, no. 1–2, p. 33–54, doi: 10.1016/S0169-555X(01)00098-8.
- Maquaire, O., Malet, J.P., Remaitre, A., Locat, J., Klotz, S., and Guillon, J., 2003, Instability conditions of marly hillslopes: Towards landsliding or gullying? The case of the Barcelonnette Basin, south east France: *Engineering Geology*, v. 70, no. 1–2, p. 109–130, doi: 10.1016/S0013-7952(03)00086-3.
- McKean, J., and Roering, J., 2004, Objective landslide detection and surface morphology mapping using high-resolution airborne laser altimetry: *Geomorphology*, v. 57, no. 3–4, p. 331–351, doi: 10.1016/S0169-555X(03)00164-8.
- McLaughlin, R.J., Kling, S.A., Poore, R.Z., McDougall, K., and Beutner, E.C., 1982, Post–Middle Miocene accretion of Franciscan rocks, northwestern California: *Geological Society of America Bulletin*, v. 93, no. 7, p. 595–605, doi: 10.1130/0016-7606(1982)93<595:PMAOFR>2.0.CO;2.
- McLaughlin, R.J., Ellen, S.D., Blake, M.C.J., Jayko, A.S., Irwin, W.P., Aalto, K.R., Carver, G.A., and Clark, S.H.J., 2000, Geology of the Cape Mendocino, Eureka, Garberville, and Southwestern Part of the Hayfork 30 × 60 Minute Quadrangles and Adjacent Offshore Area, Northern California: U.S. Geological Survey Miscellaneous Field Studies Map MF-2336, 1:100 000 scale.
- McSaveney, M.J., and Griffiths, G.A., 1987, Drought, rain, and movement of a recurrent earthflow complex in New Zealand: *Geology*, v. 15, no. 7, p. 643–646, doi: 10.1130/0091-7613(1987)15<643:DRAMO>2.0.CO;2.
- Merritts, D., and Bull, W.B., 1989, Interpreting Quaternary uplift rates at the Mendocino triple junction, northern California, from uplifted marine terraces: *Geology*, v. 17, no. 11, p. 1020–1024, doi: 10.1130/0091-7613(1989)017<1020:1QURAT>2.3.CO;2.
- Muhs, D.R., Thorson, R.M., Clague, J.J., Mathews, W.H., McDowell, P.F., and Kelsey, H.M., 1987, Pacific Coast and mountain system, in Graf, W.L., ed., *Geomorphic Systems of North America*: Boulder, Colorado, Geological Society of America, p. 517–581.
- Nolan, K.M., and Janda, R.J., 1995, Movement and Sediment Yield of Two Earthflows, Northwestern California: U.S. Geological Survey Professional Paper 1454, no. F, p. F1–F12.
- Ohlmacher, G.C., 2007, Plan curvature and landslide probability in regions dominated by earth flows and earth slides: *Engineering Geology*, v. 91, no. 2–4, p. 117–134, doi: 10.1016/j.enggeo.2007.01.005.
- Palmquist, R.C., and Bible, G., 1980, Conceptual modeling of landslide distribution in time and space: *Bulletin of the International Association of Engineering Geology*, v. 21, p. 178–186, doi: 10.1007/BF02591559.
- Perron, J.T., Kirchner, J.W., and Dietrich, W.E., 2009, Formation of evenly spaced ridges and valleys: *Nature*, v. 460, no. 7254, p. 502–505, doi: 10.1038/nature08174.
- Pettinga, J.R., 1987, Waipoapa landslide—A deep-seated complex block slide in Tertiary weak-rock flysch, southern Hawkes Bay, New Zealand: *New Zealand Journal of Geology and Geophysics*, v. 30, no. 4, p. 401–414.
- Putnam, W.C., and Sharp, R.P., 1940, Landslides and earthflows near Ventura, southern California: *Geographical Review*, v. 30, no. 4, p. 591–600, doi: 10.2307/210535.
- Roering, J.J., Stimely, L.L., Mackey, B.H., and Schmidt, D.A., 2009, Using DInSAR, airborne LiDAR, and archival air photos to quantify landsliding and sediment transport: *Geophysical Research Letters*, v. 36, L19402, 5 p., doi: 10.1029/2009GL040374.
- Savage, W., and Wasowski, J., 2006, A plastic flow model for the Acquara-Vadoncello landslide in Senerchia, southern Italy: *Engineering Geology*, v. 83, no. 1–3, p. 4–21, doi: 10.1016/j.enggeo.2005.06.024.
- Savage, W.Z., and Chleborad, A.F., 1982, A model for creeping flow in landslides: *Bulletin of the Association of Engineering Geologists*, v. 19, no. 4, p. 333–338.
- Schulz, W.H., 2007, Landslide susceptibility revealed by LIDAR imagery and historical records, Seattle, Washington: *Engineering Geology*, v. 89, no. 1–2, p. 67–87, doi: 10.1016/j.enggeo.2006.09.019.
- Schulz, W.H., Kean, J.W., and Wang, G.H., 2009a, Landslide movement in southwest Colorado triggered by atmospheric tides: *Nature Geoscience*, v. 2, no. 12, p. 863–866, doi: 10.1038/ngeo0659.
- Schulz, W.H., McKenna, J.P., Kibler, J.D., and Biavati, G., 2009b, Relations between hydrology and velocity of a continuously moving landslide—Evidence of pore-pressure feedback regulating landslide motion?: *Landslides*, v. 6, no. 3, p. 181–190, doi: 10.1007/s10346-009-0157-4.
- Schwab, M., Rieke-Zapp, D., Schneider, H., Liniger, M., and Schlunegger, F., 2008, Landsliding and sediment flux in the central Swiss Alps: A photogrammetric study of the Schimbrig landslide, Entlebuch: *Geomorphology*, v. 97, no. 3–4, p. 392–406, doi: 10.1016/j.geomorph.2007.08.019.
- Scott, R.G., 1973, *Geology and Sediment Production for Ten Eel River Landslides*: Red Bluff, CA, California Department of Water Resources, Northern District, Memorandum Report, 29 p.
- Skempton, A.W., 1964, Long-term stability of clay slopes: *Geotechnique*, v. 14, p. 77–102, doi: 10.1680/geot.1964.14.2.77.
- Slama, C.C., 1980, *Manual of Photogrammetry*: Falls Church, Virginia, American Society of Photogrammetry, 1056 p.
- Slatton, K.C., Carter, W.E., Shrestha, R.L., and Dietrich, W., 2007, Airborne laser swath mapping: Achieving the resolution and accuracy required for geosurficial research: *Geophysical Research Letters*, v. 34, no. 23, L23S10, 5 p., doi: 10.1029/2007GL031939.
- Sloan, J., Miller, J.R., and Lancaster, N., 2001, Response and recovery of the Eel River, California, and its tributaries to floods in 1955, 1964, and 1997: *Geomorphology*, v. 36, no. 3–4, p. 129–154, doi: 10.1016/S0169-555X(00)00037-4.
- Smith, B.J., Tilton, W.C., Elko, J.M., and Jacobus, C.D., 1974, Eel River Basin Environmental Studies: Red Bluff, California, California Department of Water Resources, Northern District, 93 p.
- Sommerfield, C.K., and Wheatcroft, R.A., 2007, Late Holocene sediment accumulation on the northern California shelf: Oceanic, fluvial, and anthropogenic influences: *Geological Society of America Bulletin*, v. 119, no. 9–10, p. 1120–1134, doi: 10.1130/B26019.1.
- Sommerfield, C.K., Drake, D.E., and Wheatcroft, R.A., 2002, Shelf record of climatic changes in flood magnitude and frequency, north-coastal California: *Geology*, v. 30, no. 5, p. 395–398, doi: 10.1130/0091-7613(2002)030<0395:SROCCI>2.0.CO;2.
- Stark, C.P., and Guzzetti, F., 2009, Landslide rupture and the probability distribution of mobilized debris volumes: *Journal of Geophysical Research—Earth Surface*, v. 114, F00A02, 16 p., doi: 10.1029/2008JF001008.
- Stark, C.P., and Hovius, N., 2001, The characterization of landslide size distributions: *Geophysical Research Letters*, v. 28, no. 6, p. 1091–1094, doi: 10.1029/2000GL008527.
- Stock, J.D., and Dietrich, W.E., 2006, Erosion of steepland valleys by debris flows: *Geological Society of America Bulletin*, v. 118, no. 9–10, p. 1125–1148, doi: 10.1130/B25902.1.
- Swanson, F.J., and Swanson, D.N., 1977, Complex mass-movement terrains in the western Cascade Range, Oregon: *Geological Society of America Reviews in Engineering Geology*, v. 3, p. 113–124.
- Swanson, D.N., Ziemer, R.J., and Janda, R.J., 1995, Rate and mechanics of progressive hillslope failure in the Redwood Creek basin, northwestern California, in Nolan, K.M., Kelsey, H.M., and Marron, D.C., eds., *Geomorphic Processes and Aquatic Habitat in the Redwood Creek Basin, Northwestern California*: U.S. Geological Survey Professional Paper 1454, p. E1–E16.
- ten Brink, U.S., Barkan, R., Andrews, B.D., and Chaytor, J.D., 2009, Size distributions and failure initiation of submarine and subaerial landslides: *Earth and Planetary Science Letters*, v. 287, no. 1–2, p. 31–42, doi: 10.1016/j.epsl.2009.07.031.
- van Asch, T.W.J., Van Beek, L.P.H., and Bogaard, T.A., 2007, Problems in predicting the mobility of slow-moving landslides: *Engineering Geology*, v. 91, no. 1, p. 46–55, doi: 10.1016/j.enggeo.2006.12.012.
- Van Den Eeckhaut, M., Poesen, J., Verstraeten, G., Vanacker, V., Moeyersons, J., Nyssen, J., and van Beek, L.P.H., 2005, The effectiveness of hillshade maps and expert knowledge in mapping old deep-seated landslides: *Geomorphology*, v. 67, no. 3–4, p. 351–363, doi: 10.1016/j.geomorph.2004.11.001.
- Van Den Eeckhaut, M., Poesen, J., Verstraeten, G., Vanacker, V., Nyssen, J., Moeyersons, J., van Beek, L.P.H., and Vandekerckhove, L., 2007, Use of LIDAR-derived images for mapping old landslides under forest: *Earth Surface Processes and Landforms*, v. 32, no. 5, p. 754–769, doi: 10.1002/esp.1417.
- Vulliet, L., and Hutter, K., 1988, Viscous-type sliding laws for landslides: *Canadian Geotechnical Journal*, v. 25, no. 3, p. 467–477, doi: 10.1139/t88-052.
- Wheatcroft, R.A., and Sommerfield, C.K., 2005, River sediment flux and shelf sediment accumulation rates on the Pacific Northwest margin: *Continental Shelf Research*, v. 25, no. 3, p. 311–332, doi: 10.1016/j.csr.2004.10.001.
- Wieczorek, G.F., 1984, Preparing a detailed landslide-inventory map for hazard evaluation and reduction: *Bulletin of the Association of Engineering Geologists*, v. 21, no. 3, p. 337–342.
- Wills, C.J., and McCrink, T.P., 2002, Comparing landslide inventories: The map depends on the method: *Environmental & Engineering Geoscience*, v. 8, no. 4, p. 279–293, doi: 10.2113/8.4.279.
- Wolf, P.R., and Dewitt, B.A., 2000, *Elements of Photogrammetry, with Applications in GIS*: Boston, Massachusetts, McGraw-Hill, 624 p.
- Zhang, X.B., Phillips, C., and Marden, M., 1991a, Internal deformation of a fast-moving earthflow, Raukumara Peninsula, New Zealand: *Geomorphology*, v. 4, no. 2, p. 145–154, doi: 10.1016/0169-555X(91)90025-6.
- Zhang, X.B., Phillips, C., and Pearce, A., 1991b, Surface movement in an earthflow complex, Raukumara Peninsula, New Zealand: *Geomorphology*, v. 4, no. 3–4, p. 261–272, doi: 10.1016/0169-555X(91)90009-Y.

MANUSCRIPT RECEIVED 26 MARCH 2010
 REVISED MANUSCRIPT RECEIVED 10 OCTOBER 2010
 MANUSCRIPT ACCEPTED 12 OCTOBER 2010

Printed in the USA